Available online at www.sciencedirect.com

ScienceDirect

Underground Space 4 (2019) 147–167

www.elsevier.com/locate/undsp

Evaluation of seismic behavior of box culvert buried in the ground through centrifuge model tests and numerical analysis

Hitoshi Yatsumoto [a,*], Yasuo Mitsuyoshi [b], Yasuo Sawamura [c], Makoto Kimura [c]

[a] *Maintenance Division, Hanshin Expressway Company Limited, Japan*
[b] *Obayashi Corporation, Construction Division, Japan*
[c] *Department of Civil and Earth Resources Engineering, Kyoto University, Japan*

Received 19 March 2018; received in revised form 18 September 2018; accepted 23 September 2018
Available online 18 December 2018

Abstract

Japan has yet to establish a seismic design for road box culverts (RBCs) because past major earthquakes did not damage them. In recent years, structures with enlarged sectional dimensions (the purpose of which is to optimize the internal space in RBCs) have become common. However, the unknown seismic strength of such large RBCs makes RBC seismic designs increasingly necessary. Several seismic design methods have been developed for and applied to rectangular underground structures, e.g., cut-and-cover tunnels, which are structurally similar to RBCs. Although these methods are applicable to RBCs, it is uncertain whether they can be applied directly because there are currently no evaluation results from model tests on RBCs, which have unique structural features, e.g., no haunch at the bottom of the sidewalls. Therefore, we verify a seismic behavior of an RBC and develop a method for evaluating it in order to establish a seismic design for RBCs. We conducted centrifuge model tests subjected to seismic force and a numerical analysis using an elastoplastic finite analysis method, in addition, we validated this analysis by comparing the test and analytical results. The test results show RBCs will most likely develop rocking rotation when the ground strain exceeds approximately 0.08%. A comparison of the numerical and experimental results shows that this analysis can estimate the shear deformation behavior with approximately 90% accuracy in square cross-section cases. Meanwhile, this analysis has tendency to underestimate the axial forces in each case and to overestimate the bending moments of some members in the case of wide cross-sections.

Keywords: Box culvert; Centrifuge model test; Numerical analysis; Shear deformation; Rocking rotation

1 Introduction

In Japan, road box culverts (RBCs) are typically designed on the basis of the Road Earthwork and Culvert Construction Guiding Principle (Japan Road Associations, 2010), hereinafter referred to as the guiding principle. In this context, an RBC refers to a BC whose internal space is used as a road. The guiding principle refers to a culvert with a traditional structure as a conventional culvert and determines its application range (e.g., in the case of a cast-in-place RBC, the maximum width, height, and overburden are 6.5, 5, and 20 m, respectively, and the structure must be of single-box type). Furthermore, this guiding principle states that conventional culverts satisfying these structural conditions are considered to exhibit a seismic performance, even without a seismic design; it is possible to determine these structural conditions solely with a static design. This is because when an earthquake occurs, RBCs are thought to behave in unison with the surrounding ground, and therefore, the lining is not subjected to large seismic forces. Another reason is that past major earthquakes did not damage RBCs. Even after earthquakes that have caused serious damage to geotechnical structures

* Corresponding author.
E-mail address: hitoshi-yatsumoto@hanshin-exp.co.jp (H. Yatsumoto).

https://doi.org/10.1016/j.undsp.2018.09.007

(e.g., the Niigata Prefecture Chuetsu-oki Earthquake in 2007, the Great East Japan Earthquake in 2011, and the Kumamoto Earthquake in 2016), no significant damage to RBCs was reported (EJECI, 2016; Murakami, 2011; NILIM and PWRI, 2004; Toyota, 2007).

In recent years, structures with enlarged sectional dimensions (the purpose of which, in RBCs, is to optimize the internal space) have become common. As that these structures do not meet the aforementioned structural conditions of conventional culverts, they require not only a static design but also a seismic design, creating the need for a method that can be applied to RBCs. However, there is no standard seismic design methodology because of the absence of data regarding major damage caused by past earthquakes. Several seismic design methods have been applied to rectangular underground structures, e.g., cut-and-cover tunnels, which are structurally similar to RBCs, and various researchers have developed ways to evaluate their seismic behavior and seismic design (Abuhajar, El Naggar, & Newson, 2015; Debiasi, Gajo, & Zonta, 2013; Huo, Bobet, Fernández, & Ramirez, 2006; Hushmand et al., 2016; Penzien, 2000; Tsinidis, 2017; Tsinidis, Rovithis, Pitilakis, & Chazelas, 2016; Wang, 1993). It is presumed that the results of those studies are also applicable to the seismic design of RBCs because the cross-section of RBCs and the material of members of RBCs are similar to the underground structures described above.

However, RBCs have unique structural features, e.g., no haunch at the bottom of the sidewalls and a wide cross-section. Although there have been previous experimental studies (Abuhajar et al., 2015; Tsinidis et al., 2016) and validation of dynamic analyses has been conducted in this area, these studies investigated BCs of a square cross-section with no haunch at either the top or the bottom of the sidewalls. The structural features of these BCs differ from those of RBCs. Having no haunch at the bottom of the sidewalls can lead to a different damage process and failure mode under a seismic load. There exists an accuracy issue in the analysis using beam elements, namely, that the earth pressure and the seismic force may act at different places in the numerical model and an actual RBC has a wide cross-section and comprises thick members. As beam elements, ordinarily used in the dynamic analysis of underground structures, are placed in the axis position, the distance between a beam element and the edge of the cross-section where actual forces act increases as the cross-section becomes thicker. In the case of structures comprising thin members, the accuracy issue becomes negligible because the distance leading to discrepancy in the earth pressure and seismic force between the actual structure and the numerical model is small. Meanwhile, in the case of structures comprising thick members (e.g., Case 3 of this test), the accuracy issue becomes large because the distance leading to discrepancy between them is large. Therefore, it is an open question as to whether numerical analysis using beam elements can be applied to RBCs composed of thick members. These unsolved concerns also include the question as to whether the methods used in previous research can be directly applied to RBCs.

Therefore, some studies (Yamaki, Tanimoto, & Sasaki, 2011; Yatsumoto et al., 2015) have been carried out to establish a seismic design that can be applied to RBCs. In previous research (Yatsumoto et al., 2015), we conducted cyclic loading tests and numerical analysis on a specimen considering the structural features of an RBC. In that research, the damage process leading to collapse was observed carefully and the numerical analysis was verified by comparing its predictions with the experimental results. That comparison showed that numerical analysis using a model that considers the effect of a haunch can evaluate the shear deformation behavior correctly and can be used to evaluate the seismic behavior of RBCs. However, culvert models used in the test were not set in the ground but in the air. Therefore, the earth pressure to which RBC members were subjected differed between models and actual RBCs, which are usually set in an embankment or underground. We think that this evaluation for RBCs' seismic behavior is not sufficient because of this difference. Meanwhile, Yamaki et al. (2011) researched RBCs experimentally under the same earth pressures as actual RBCs; they observed shear deformation and rocking rotation (RR) but did not evaluate the seismic behavior. As such, no method has been established to evaluate RBCs under seismic motion.

Therefore, in the present study, we conducted centrifuge model tests with a scale model considering RBC structural features to verify the seismic behavior of buried RBCs and establish a way to evaluate their seismic behavior, which was not covered in previous research. In these dynamic loading tests, we designed a model ground (i.e., the sandy ground surrounding an RBC created using dry Toyoura sand) and an RBC inside a shear soil chamber, reproduced the earth pressure acting on the existing structure by means of a centrifugal force-loading device, and subjected the model to seismic force. Moreover, we conducted a numerical analysis using an elastoplastic finite analysis method and validated this analysis by comparing the test and analytical results. This paper presents the experimental and numerical results and refers to the applicability of the numerical analysis employed herein.

2 Scale model tests with a centrifugal force-loading device

2.1 Test outline

We conducted a series of centrifuge model tests using the centrifugal force-loading device belonging to the Disaster Prevention Research Institute of Kyoto University in Japan. The effective beam length of the centrifuge device was 2.5 m, the maximum centrifugal acceleration was either 200 g (at static loading) or 50 g (at dynamic loading), and the maximum centrifuge load was 24 g·t. Table 1 lists the specifications of the centrifugal force-loading device.

Figure 1 shows a chart that correlates the overburden and the cross-sectional shape (W/H) of RBCs designed in

Table 1
Specifications of centrifugal force-loading device.

Specification	Geotechnical centrifuge (DPRI)
Effective rotation radius (m)	2.5
Effective space for model installation (m)	$0.80(L) \times 0.36(W) \times 0.80(H)$
Experimental capacity (g ton)	24
Maximum centrifuge acceleration (g)	200 for static test 50 for dynamic test
Maximum number of rotations (r/min)	260

Table 2
Structural conditions of test cases.

Test case name	Overburden (m)	Inner hollow width (m)	Inner hollow height (m)	W/H
Case 1	1.0	5.0	5.0	1.0
Case 2	6.0	5.0	5.0	1.0
Case 3	1.0	15.0	5.0	3.0

the past and their relationship with the present test cases. The cross-sectional shape (W/H) shown in Fig. 1 was obtained by dividing the RBC width by the height. The cross-sectional shape and overburden were estimated from the correlation of the structural conditions of 282 RBCs prepared by Yatsumoto et al. (2015). We define this area (where most plotted points are included) as the usage range of RBCs. Based on the relationship shown in Fig. 1, the test cases for three structural conditions were selected from the usage range of structural conditions. Case 1 is a basic culvert; it has a square cross-section and a small overburden. Case 2 is a culvert constructed at a depth to investigate the influence of the overburden. Case 3 is a culvert made with a wide cross-section to investigate the influence of the cross-sectional shape. The height of the inner space is same for all the cases, and the width of Cases 1 and 2 is different from that in Case 3. In addition, the thickness of the culvert is different in all the cases owing to the difference in overburden and width of culvert. Therefore, the height and width are different for all the three cases. Figure 1 shows the structural conditions of previous experimental tests (Abuhajar et al., 2015; Tsinidis et al., 2016; Yamaki et al., 2011), as described in Section 1, which are expected to be helpful in considering the present test results. Table 2 lists the structural conditions of the present test cases. Figure 1 shows the conditions of RBCs, which can determine the structural conditions even without a seismic design. The structural dimensions for the three cases were determined using a static design and are given in Fig. 2. As seen in the figure, the haunches at the bottom slab were omitted in all models. This is one of the aforementioned RBC structural specifications.

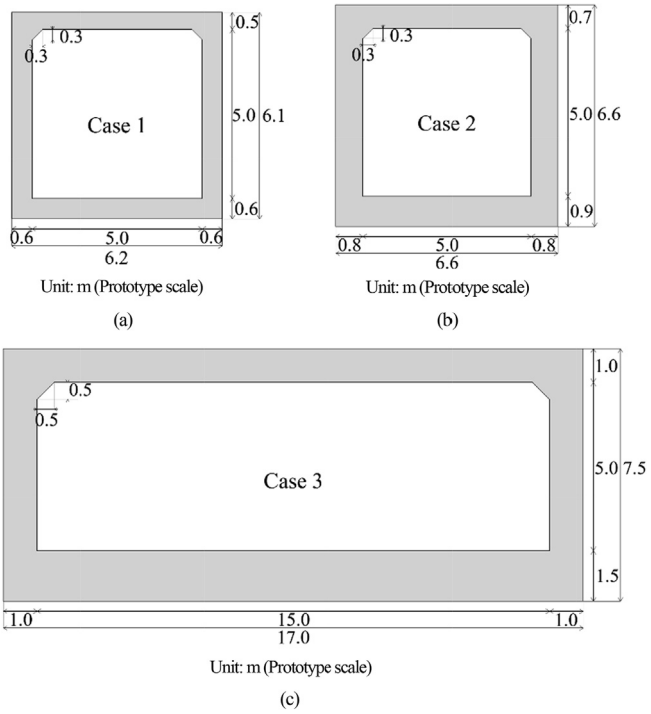

Fig. 2. Structural dimensions in (a) Case 1, (b) Case 2, and (c) Case 3.

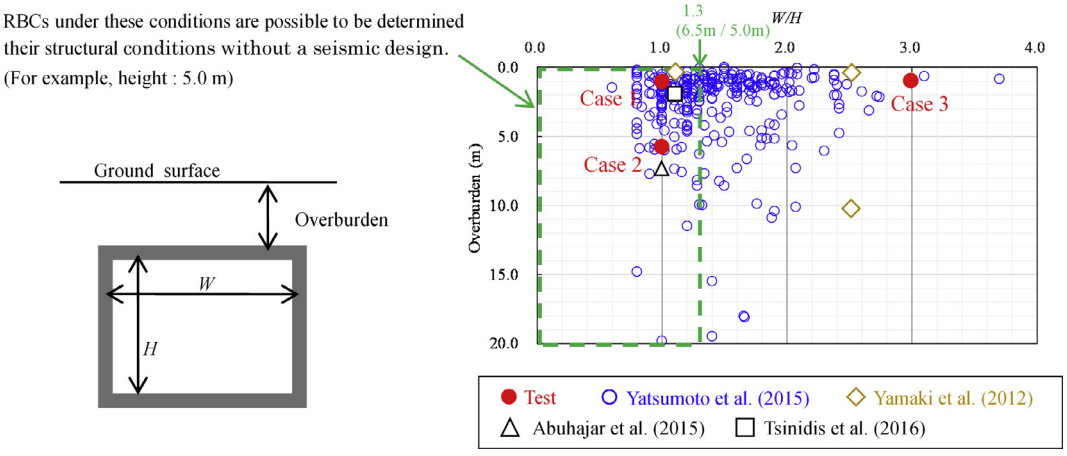

Fig. 1. Correlation between overburden and cross-sectional shape (W/H).

It would have been difficult to construct the 1/50-scale RBC model using reinforced concrete (RC), i.e., the actual material of BCs, because of the difficulty of arranging the 1/50-scale rebar. Therefore, we constructed the scaled model using aluminum instead of RC. When structures made of RC are modeled using aluminum, it is necessary to reduce the thickness of members, in order to compensate for the difference in material stiffness between aluminum and RC models. The aluminum model exhibits elasticity under the excitation condition; however, the RC model shows nonlinear behavior under the same condition. In other words, there is a difference in lateral stiffness between both models during an earthquake. It is desirable to consider the lateral stiffness of the RC model under the nonlinear behavior to accurately investigate the seismic behavior of RBCs and ground. It is impossible to determine the nonlinear behavior of a real BC made from RC during a high-magnitude earthquake. We determined the RC model dimensions via the static design and reduced the thickness of members by taking the difference in material stiffness into consideration, as mentioned above. We further reduced the thickness by taking the nonlinear behavior of the earthquake into consideration, as mentioned above. Nonlinear pushover analysis was carried out to take the nonlinear behavior of the RC model into consideration, and we determined the reduced lateral stiffness of the RC model in the case of an earthquake. We intend to consider the difference in material stiffness in another study, but consideration of further reduction in stiffness due to an earthquake is the novelty of our study. In the pushover analysis, the culvert members were modeled using the Axial-Force Dependent (AFD) model (Zhang & Kimura, 2002), which can consider the axial-force dependency according to the variable axial force of the structure and the reduced stiffness of RC under a large deformation. A horizontal load was applied to the left edge of the top slab in this pushover analysis.

Figure 3(a) outlines the pushover analysis. Figure 3(b) and (c) illustrate the connection model at the corner with and without a haunch, respectively, which was used and evaluated by Yatsumoto et al. (2015). Aluminum models were used in previous experimental research, and the difference between the aluminum and RC models was considered. However, it is not clear whether the nonlinear behavior of an actual RBC under seismic motion was considered when the model dimensions were being determined.

Figure 4 shows the horizontal load–shear strain curve for each case. As the horizontal load increases, the culvert shear strain and its rate also increase. Table 3 lists the initial stiffness, the reduced stiffness (shear strain: 1%), and the stiffness-lowering rate. We will later explain why we used a shear strain of 1%. We reduced the bending stiffness

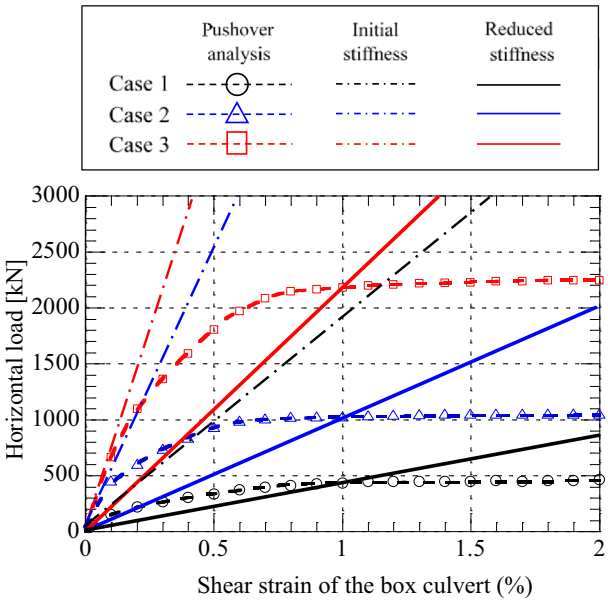

Fig. 4. Results of simulation of the road box culvert (RBC) model with pushover.

Table 3
Shear stiffness of box-culvert models.

Test case name	Initial stiffness (kN/mm)	Reduced stiffness (shear strain 1%) (kN/mm)	Stiffness-lowering rate (%)
Case 1	34.0	8.0	23
Case 2	86.0	17.4	20
Case 3	110.0	35.0	32

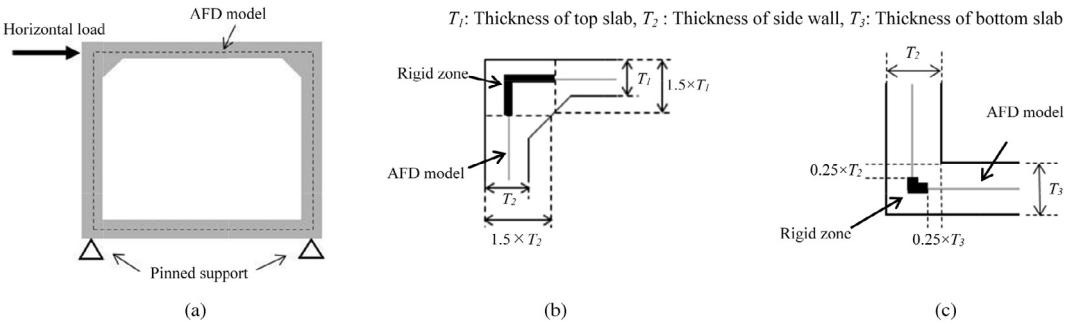

Fig. 3. Pushover analysis: (a) outline of pushover analysis, (b) corner model with haunch, and (c) corner model without haunch.

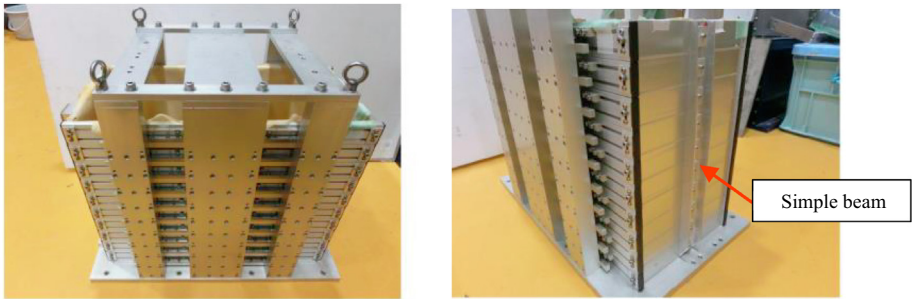

Fig. 5. Shear soil chamber: (a) front view and (b) side view.

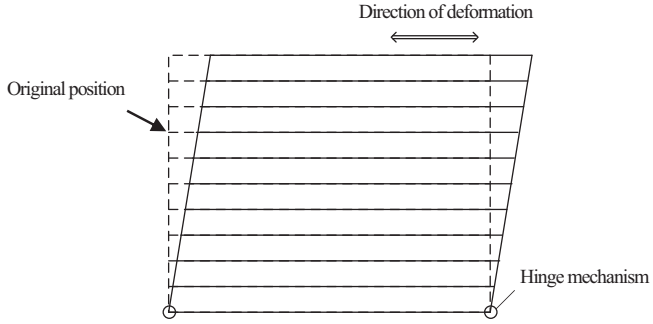

Fig. 6. Shear deformation of the shear soil chamber.

of the aluminum models using this stiffness-lowering rate and determined the structural specifications for each case.

In these tests, we used a shear soil chamber that was 500-mm wide, 230-mm deep, and 400-mm high. This chamber comprised several boxes without top and bottom slabs. The boxes were connected to a simple aluminum beam set at the outer side of the boxes, as shown in Fig. 5. Simple beams were connected to the bottom of the soil chamber using the hinge mechanism. Therefore, the soil chamber can show simple shear deformation of the model ground, as shown in Fig. 6.

Figure 7 shows one of the three 1/50-scale model cases, namely, Case 1, and the layout of the measuring instruments. The distance between the bottom of soil chamber and the surface of the bottom slab of model culvert, which touched the ground, was 140 mm in all three cases. As shown, we installed displacement sensors on the outer side of the shear soil chamber walls, acceleration meters in the ground and on the RBC, and strain gauges on the RBC. Furthermore, the earth pressure transducer (thickness of 2 mm, diameter of 7.6 mm) is installed directly on the surface of RBC. As shown in Fig. 7(b), the acceleration meters, a, b-1, c-1, and d, were placed at the center between the sidewalls of RBC and soil chamber. These meters were used to measure the horizontal acceleration time history in the ground along a vertical section. The acceleration meters, b-2 and c-2, placed at the center of the bottom or top slab were used to measure the horizontal acceleration time history at the bottom and top slab of RBC along a

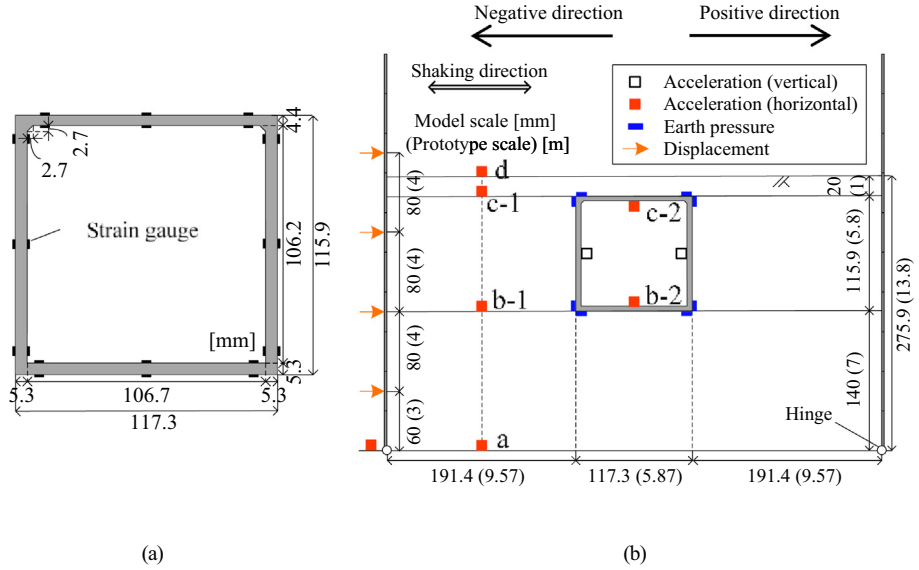

Fig. 7. Scale model of ground and RBC and layout of measuring devices in Case 1: (a) strain gauge and (b) acceleration, earth pressure, and displacement.

Table 4
Physical properties of Toyoura sand.

Specific gravity G_s	2.64
Average diameter D_{50} (mm)	0.2
Internal friction angle φ (°)	38.9
Cohesion c (kPa)	0
Maximum void ratio e_{max}	0.975
Minimum void ratio e_{min}	0.585

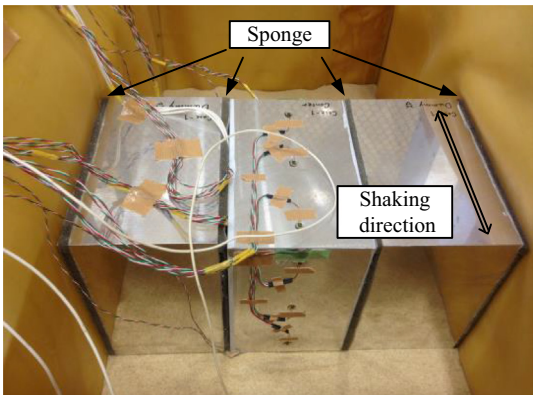

Fig. 8. RBC model divided into three pieces along the depth direction.

vertical section. b-1 and b-2 have the same height, as do c-1 and c-2. We define the right side in the figure as the positive side and the left side as the negative side. The positive bending moment is defined as bending along the direction to the inner space.

In the tests, to simulate an RBC built on a sandy ground, we created a model ground of dry Toyoura sand surrounding the RBC. Table 4 lists the physical properties of Toyoura sand. Given that the aforementioned guiding principle stipulates that the foundation ground into which an RBC will be installed must be of high quality, Toyoura sand was pluviated into the shear soil chamber to achieve a uniform soil layer with a relative density of Dr ≈ 85%.

In shaking table tests, the influence of friction between the chamber and the RBC models must be mitigated. Therefore, the RBC model was divided into three parts in the depth direction, and sponge tapes were installed among the models as well as between the models and the walls of the chamber, as shown in Fig. 8. Therefore, we assume that this test model can be treated as a two-dimensional model.

We used double-sided tape to coat the outer surface of the model with fine sand to generate the friction force between the scaled model and the surrounding soil. We set a thin rubber membrane between the shear soil chamber sidewalls and the model ground to prevent the soil from escaping the shear soil chamber. We believe that a certain amount of friction was generated (i) between the scaled model and the soil and (ii) between the soil and the sidewalls.

2.2 Waveform of input earthquake motion

Because the present tests aimed to determine the response of an RBC during a strong earthquake, we determined the shaking intensity so that the maximum shear strain of the ground would reach approximately 1%. Given that Hamada and Ohmachi (1996) reported the shear strain of the nonliquefied soil in the Great Hanshin Earthquake of 1995 to have been approximately 1%, we set the target value for the response shear strain in the present study to be 1%. As mentioned above, this is why we used a stiffness-lowering rate of 1% for the shear strain.

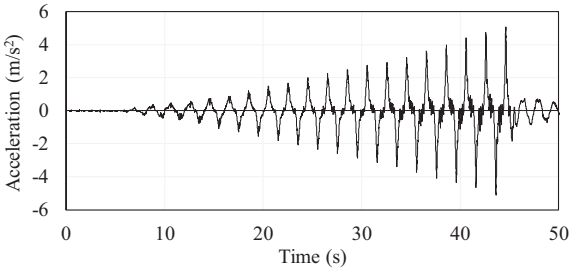

Fig. 9. Time-history acceleration waveform of input motion in Case 1.

We used 20 sine waves with a frequency of 0.5 Hz as the input earthquake waves. We increased the wave amplitude gradually until the ground shear strain became approximately 1%. The acceleration waveform consequently measured at the shaking table is shown in Fig. 9.

2.3 Summary of test results

Figure 10 shows the time-history waveform of the ground shear strain in each case. This strain refers to the strain obtained by dividing the amount of relative deformation by 80 mm (4.0 m in prototype scale), which is the distance between the heights of 140 mm (7.0 m in prototype scale) from the shear soil chamber bottom (which corresponds to the bottom slab of the RBC) and 220 mm (11.0 m in prototype scale) from the bottom. Despite the small variation in the positive and negative sides, the shear strain reached the target value of 1% in all cases.

Figure 11 shows the results of the spectral analysis of the response acceleration obtained at acceleration measurement points a, b-1, and c-1 in the ground. The upper charts show the results of the spectral analysis at each measurement point, and the lower charts show the spectrum amplification rate calculated by dividing the spectrum values of points b-1 and c-1 by the spectrum value of point a considering the spectrum amplification from the bottom of the shear soil chamber. In all cases, a large spectrum was observed to occur at frequencies corresponding to odd multiples of 0.5 Hz, such as 0.5, 1.5, and 2.5 Hz, and so on. In all cases, especially in Cases 2 and 3, the amplification rate at frequency bands above 3 Hz was high. In Case 3, the frequency range of amplification expanded to approximately 10 Hz, and the amplification rate was significantly higher than that in the other cases. A possible reason for this spectrum amplification at high frequencies is the interference of waves that propagate from the shear soil chamber walls, which correspond to the lateral boundary.

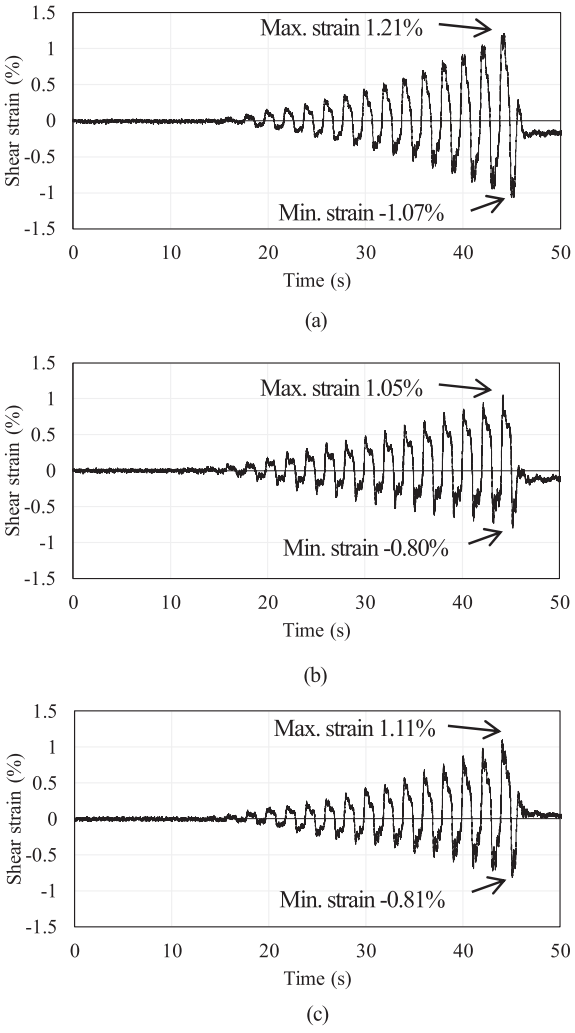

Fig. 10. Time-history waveform of ground shear strain in (a) Case 1, (b) Case 2, and (c) Case 3.

In Case 3, because the RBC was wide and the distance to the lateral boundary was short, the influence of this lateral boundary was large, which possibly caused amplification over a wide range of frequencies, as observed in the results for Case 3.

Based on the eigenvalue analysis, using the numerical analysis described in the next section, the first natural frequency is ~1.3 Hz and the second natural frequency is ~3.2 Hz despite slight deviations among the three cases. We found that the shear deformation of the ground and the RBC is unaffected by high frequencies in excess of the second natural frequency. We obtained the acceleration distribution after using a filter to eliminate all frequencies higher than 5 Hz.

Figure 12 shows the distribution of acceleration values in the positive direction at each shaking level (ground shear strain values: 0.25%, 0.5%, 0.75%, and 1.0%). The solid and dotted lines show the ground and RBC responses, respectively. Although the distribution is shaped differently in each case, in all cases, the distributions of the ground and RBC response acceleration values show discrepancy from a small ground strain value as small as 0.25%. The fact that the ground and RBC acceleration values do not coincide indicates that they might be independent of each other because of the RR, which has been confirmed in previous experimental research conducted by Yamaki et al. (2011) on an RBC.

To determine how RBCs behave when shaken, we summarize the variations in the bending moment, axial force, and earth pressure in the positive direction at each shaking level. Figure 13 shows the distributions in the static state (results of Cases 1, 2, and 3) and when the shear strain of the surrounding ground reached 0.25%, 0.50%, 0.75%, and 1.0%. As shown in Fig. 13, the distribution of bending moment in the static state has an almost symmetric shape,

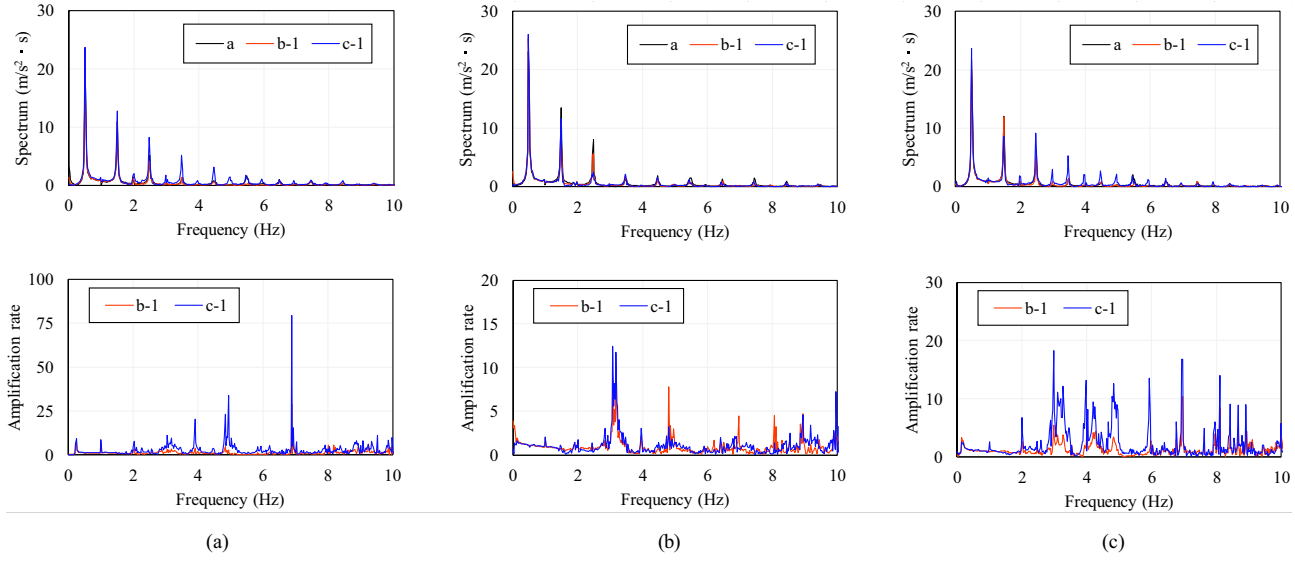

Fig. 11. Spectral analysis of ground response acceleration in (a) Case 1, (b) Case 2, (c) and Case 3.

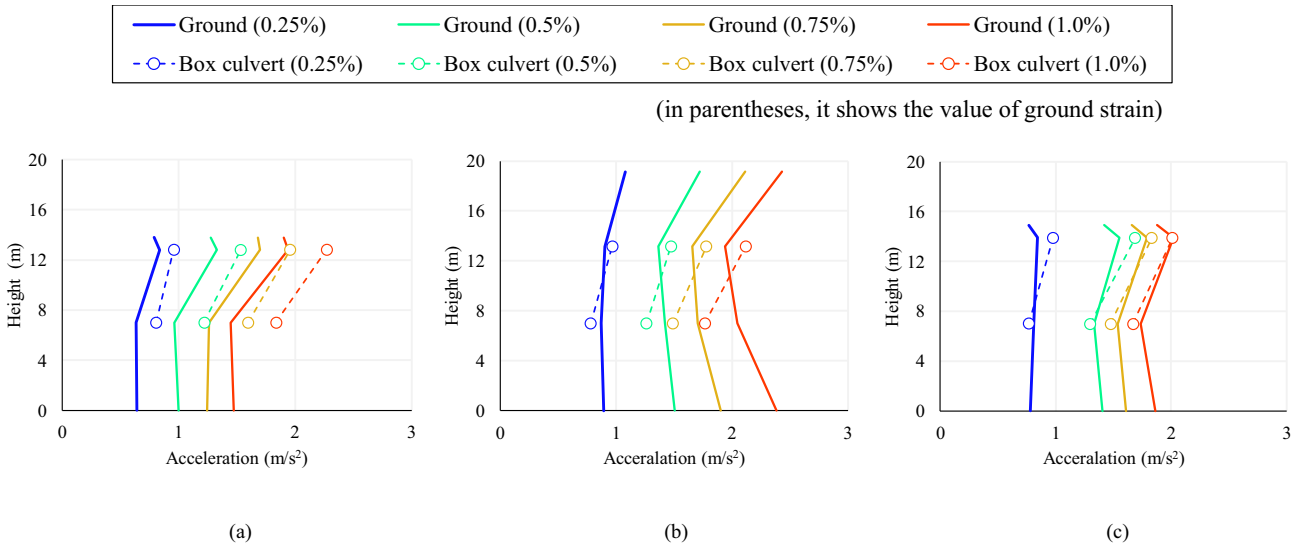

Fig. 12. Distribution acceleration at different shaking levels (positive direction) in (a) Case 1, (b) Case 2, and (c) Case 3. The solid and dotted lines show the ground and RBC responses, respectively.

while the distributions of axial force and earth pressure in the static state have an asymmetric shape. We assume that one of the reasons of this is the deficiency of setting up the culvert model in the model ground. Furthermore, it is assumed that the reason for the asymmetric shape in the earth pressure is large dispersion caused by the aforementioned installing method of earth pressure transducer. However, even though such an installation method is used, we assume that a contact state between RBC and ground can be investigated accurately.

For example, the bending moments at the left-side corner of the top slab and the right-side corner of the bottom slab were observed to increase in the positive direction as the surrounding ground strain increased. We assumed that this variation in the bending moment is caused by an increase in the angle at the corner of the left end of the top slab and that at the right end of bottom slab. This occurs when the RBC exhibits shear deformation, and the cross-sectional shape becomes a right parallelogram. The distributions of both the bending moment and axial force agree well with those reported previously (Sawamura, Kishida, & Kimura, 2014; Tsinidis et al., 2016). Therefore, RBC shear deformation seems to occur in all cases. The earth pressure indicated here refers to the earth pressure in the direction orthogonal to the axis of a member. From the earth pressure distribution, we see a large increase in earth pressure at three points (the right end of the bottom slab, the top of the left-sidewall, and the bottom of the right-sidewall) and a large decrease at the left end of the bottom slab, along with an increase in the surrounding ground strain in all cases. To analyze the earth pressure, we created a time-history chart of the variation in earth pressure at each end of the bottom slab, as shown in Fig. 14.

In all cases, earth pressure at each measuring point repeatedly increases and decreases because sine waves were used as the input waves. When the earth pressure at the left end of the bottom slab increases, that at the right end decreases. Conversely, when the earth pressure at the left end of the bottom slab decreases, that at the right end increases. Moreover, the earth pressure reduces to zero, as shown Fig. 14, which is approximately 36 and 32 s in Cases 1 and 2, respectively. The noncontact state is shown when the earth pressure becomes zero. Judging from the variation in earth pressure, the noncontact between the bottom slab and ground occurred alternately at the edge of both sides of the bottom slab, probably because of the rocking rotation (RR).

Previous research (Abuhajar et al., 2015; Debiasi et al., 2013; Penzien, 2000; Tsinidis et al., 2016; Tsinidis, 2017; Wang, 1993) focusing on a rectangular underground structure suggested that both RR and shear deformation occur during earthquake motion. However, the data that show both behaviors (shear deformation and RR) could not be obtained directly in this study because the angle meter is not used to obtain the shear deformation and RR angles. Therefore, we calculated shear deformation and RR angles using numerical analysis and verified the behaviors.

3 Numerical analysis

3.1 Numerical analysis method

To examine the method for evaluating RBCs during an earthquake and understand shear deformation and RR, which could not be directly measured using the aforementioned centrifuge model tests, we simulated the centrifuge model tests using a two-dimensional elastoplastic finite-

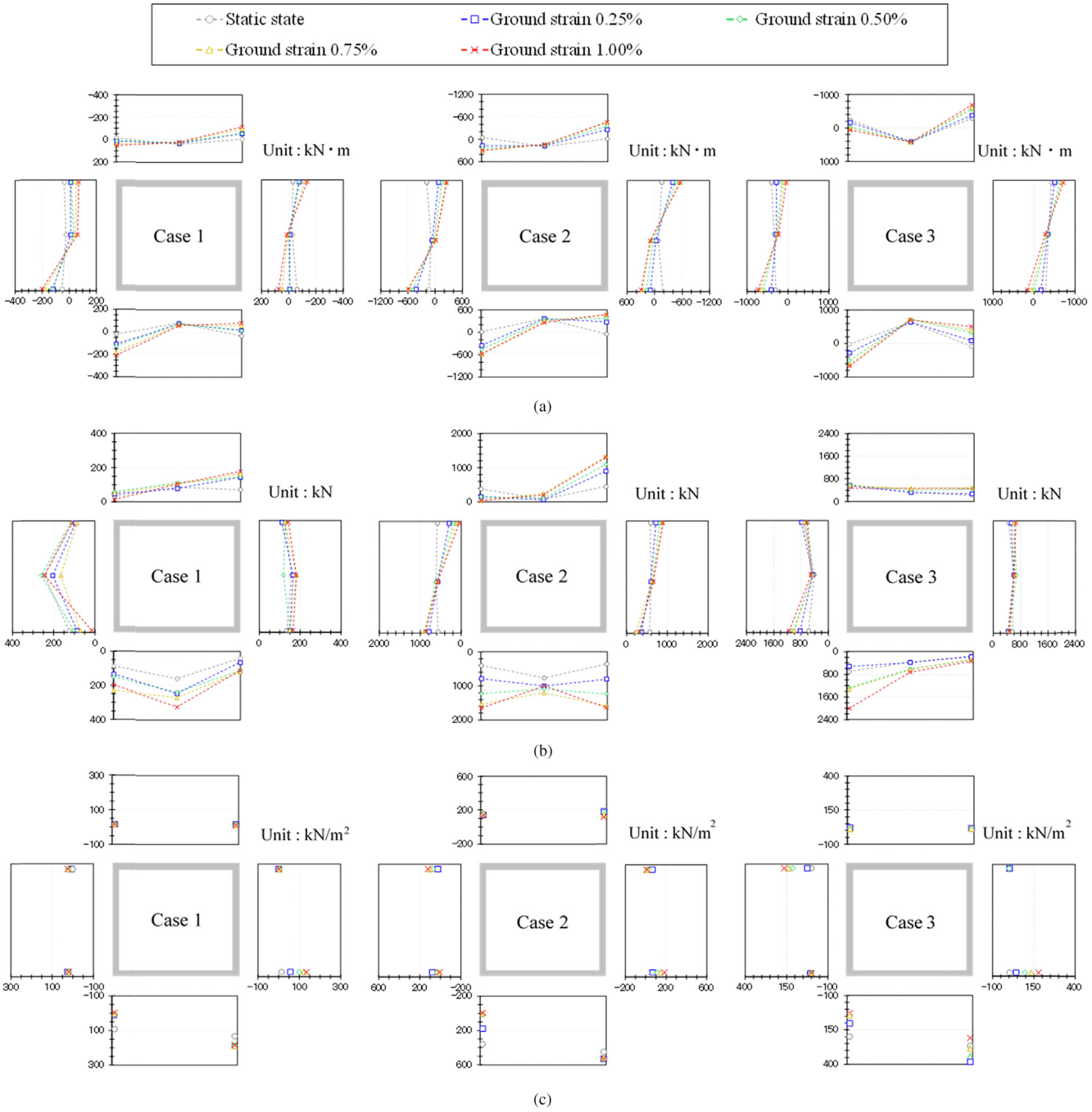

Fig. 13. Variations in bending moment, axial force, and earth pressure: (a) bending moment (left: Case 1, center: Case 2, right: Case 3); (b) axial force (left: Case 1, center: Case 2, right: Case 3); and (c) earth pressure (left: Case 1, center: Case 2, right: Case 3).

element method, as implemented in the DBLEAVES analysis code. DBLEAVES performs numerical analysis based on the infinitesimal deformation theory and the three-dimensional elastoplastic finite-element analysis code DGPILE3D developed by Kimura and Zhang (2000). It was improved by Ye, Ye, Zhang, and Yashima (2007) and can be applied to problems involving large deformations. The accuracy and applicability of DBLEAVES has been verified through its use with many other underground structures, such as pile foundations (Danno & Kimura, 2009; Jin, Bao, Kondo, & Zhang, 2010), tunnels (Cui, Kishida, & Kimura, 2010; Xia, Ye, Wang, Ye, & Zhang, 2010), and arch culverts (Sawamura, Ishihara, Kishida, & Kimura, 2016; Sawamura, Matsushita, Kishida, & Kimura, 2017). We chose DBLEAVES as the platform for reproducing these centrifuge model tests because (i) the out-of-plane direction of the RBC does not change and (ii) the ground material used in this simulation (i.e., Toyoura sand) was used in other studies. The accuracy and applicability of these tests were confirmed.

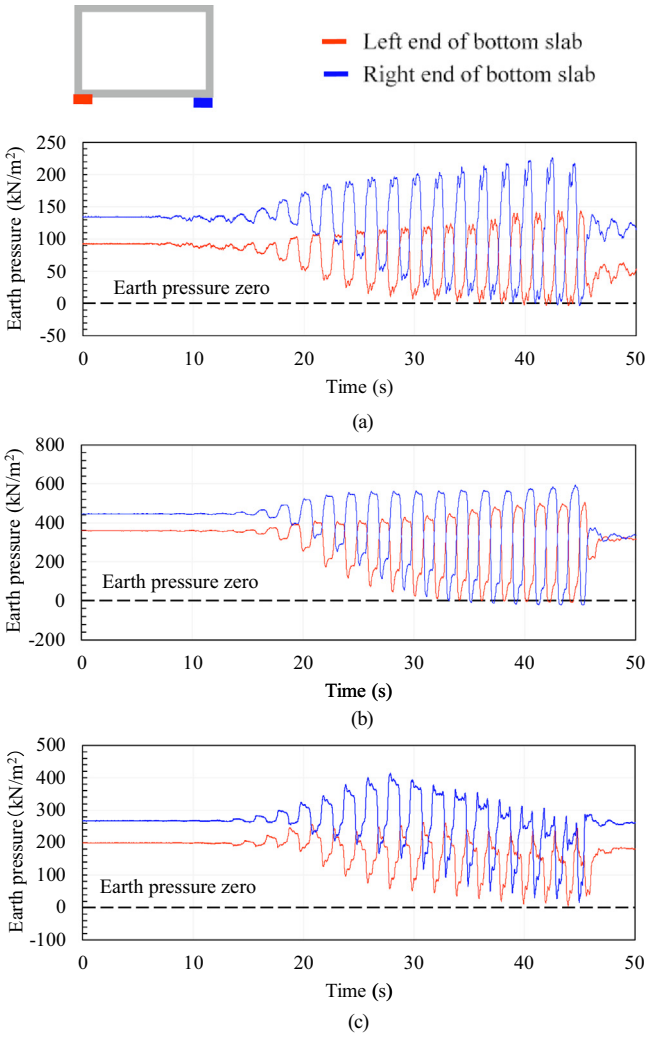

Fig. 14. Time-history variation in earth pressure in (a) Case 1, (b) Case 2, and (c) Case 3.

3.2 Analytical cases

The analytical cases comprised three centrifuge test cases. We modeled the shear soil chamber, model ground, and model RBC. Figure 15 shows the analytical mesh and boundary conditions for each case. The sidewalls of the shear soil chamber were modeled with elastic beams, and the bottom and lower ends of a sidewall were connected by a hinge to simulate the hinge mechanism of the shear soil chamber. Furthermore, the right and left-sidewalls of the actual shear soil chamber behave the same in both the x- and y-directions when shaken because both walls were connected through the out-of-plane sidewalls. Therefore, we considered an equal-displacement boundary condition at the right and left nodes with the same height, which was used to model the sidewalls of the soil chamber so that they would behave the same in both the x- and the y-directions. We used a fixed condition (i.e., no movement in both directions) at the shear soil chamber bottom for both the x- and the y-directions.

In this analysis, we used stiffness proportional damping, with h (damping coefficient) being 0.05 for the soil elements and 0.02 for the RBC elements. The integration time interval was set at 0.005 s using the Newmark-β method ($\beta = 1/4$; $\gamma = 1/2$). Moreover, we applied the same input acceleration as that considered in the centrifuge model tests at the bottom of the shear soil chamber.

3.3 Model of ground and culvert lining

In this dynamic analysis, we modeled the soil behavior using the subloading t_{ij} model (Nakai & Hinokio, 2004). The principal feature of this model is its ability to consider not only the influence of the intermediate principal stress and the confining pressure dependence of the shear rigidity but also the normal and overconsolidated states without any distinction between sand and clay. In addition, as the subloading t_{ij} model was developed for practical applications, we deemed this model to be superior to other models because many of the necessary parameters can be determined easily via triaxial and consolidation tests. Table 5 lists the properties of Toyoura sand used in this analysis. Model RBC was designed with an elastic beam element that is often used in the seismic analysis of underground

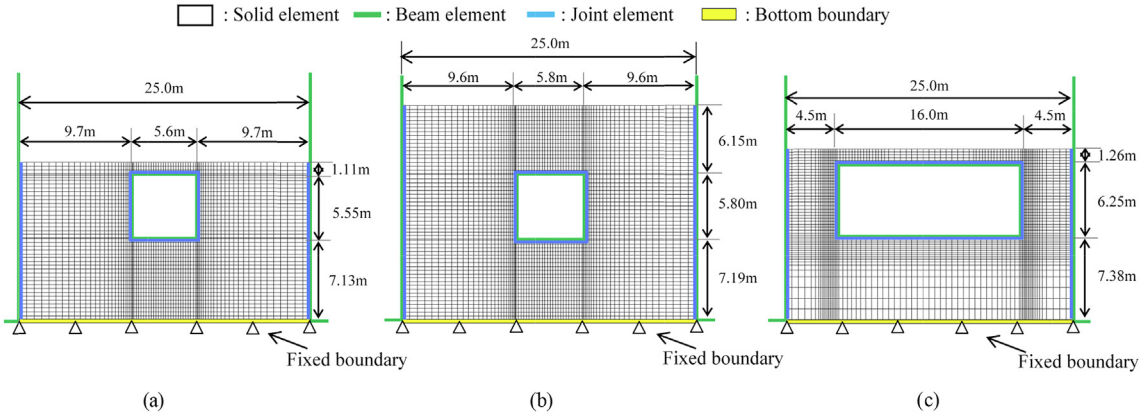

Fig. 15. Outline of models for the analysis: (a) Case 1, (b) Case 2, and (c) Case 3.

Table 5
Parameters of Toyoura Sand used in the present analysis.

Principal stress ratio at critical state $R_{cs} = (\sigma_1/\sigma_3)_{cs(comp.)}$	3.2
Compression index λ	0.07
Swelling index κ	0.004 5
$N = e_{NC}$ at $p = 98$ kPa & $q = 0$ kPa	1.1
Poisson's ratio v_e	0.271
Parameter on density and confining pressure α	60
Parameter on the form of yield surface β	2

structures. The value of Poisson's ratio with respect to ground is 0.271, as calculated from internal friction angle with value 38.9°, which is obtained from the shear strength test of Toyoura sand. In the calculation, we used Jaky's equation (Eq. (1)) and the equation (Eq. (2)) given by the theory of elasticity.

$$K_0 = 1 - \sin\varphi \tag{1}$$

$$v = K_0/(1 - K_0) \tag{2}$$

where φ is the internal friction angle, K_0 is the coefficient of earth pressure at rest, v is the Poisson's ratio.

Table 6 lists the material constants of the RBC used in this analysis. Because the RBC model was made of aluminum, as described previously, the properties of aluminum were used for the culvert in these tests. The value of Poisson's ratio with respect to the culvert is 0.17, as obtained from the quality label. Furthermore, to simulate the contact state, we used joint elements (i) between the soil and the RBC and (ii) between the soil and the shear soil chamber walls. These joint elements are capable of reproducing the separation between the two parts that they connect because they generate a contact force in the normal direction of the element but do not generate a tensile force, which would allow separation. They can also simulate a situation that involves a slide in the shear direction with friction, reproducing the behavior (i) between the ground inside the shear soil chamber and the RBC and (ii) between the ground and the shear soil chamber walls. Table 7 lists the material constants of the joint elements, which are based on the results of one-plane shear tests with mortar and Toyoura sand.

Table 6
Material constants of culvert model used in the present analysis.

Young's modulus E (kN/m^2)	6.93×10^7
Density ρ (g/cm^3)	2.7
Poisson's ratio v_c	0.333

Table 7
Material constants of joint element used in the present analysis.

Shear stiffness K_s (kN/m^2)	1.55×10^7
Normal stiffness K_n (kN/m^2)	1.55×10^7
Cohesion c (kN/m^2)	5.0
Internal friction angle φ (°)	28.0

As mentioned previously, to generate the friction, the outer surface of RBCs is coated with fine sand; a rubber membrane was set between the modeled ground and the shear soil chamber sidewalls. We assume that the friction situation of modeled ground-RBC and modeled ground-soil shear chamber is similar to that of soil and mortar. Therefore, we use the coefficient of the joint element, which is obtained from the shear test conducted between the soil and mortar in a previous study, for use in this simulation. Furthermore, the influence of the values of the normal and shear stiffness, K_n and K_s, at the contact between the structure and the sand was investigated using sensitivity analysis. The result in the case in which the values of K_n and K_s were reduced to one-tenth confirmed that the rates of change of both the bending moment and the axial force were much less than 10% of the result in the case where K_n and K_s were not reduced, even in Case 2 where their rates of change were the highest.

4 Results and evaluation of numerical analysis

4.1 1-g analysis

Before carrying out a dynamic analysis, we conducted a 1-g analysis for each case. In this analysis, the soil was modeled using an elastic element. We used Young's modulus obtained from the initial shear modulus. This initial shear modulus was determined from the shear stress–shear strain curve obtained from the numerical simulation of triaxial tests on Toyoura sand using the subloading t_{ij} model. The fixities at the bottom boundaries were fixed horizontally and vertically, but those at the side boundaries were allowed to move vertically (roller hinges). Figure 16 shows the results of the 1-g analysis for the distributions of bending moments, axial forces, and earth pressure, where the results of the tests described in Section 2 are indicated by red circles.

Regarding the bending moment, the discrepancy between the numerical and experimental results for the center part of sidewalls in Case 2 is slightly larger than that in Cases 1 and 3. Meanwhile, the numerical results show good agreement with the experimental results for other parts in all cases.

Regarding the axial-force distribution, the numerical results are lower than the experimental ones in all cases, and this discrepancy is especially large at the top and bottom slabs. In Case 3, at the point where the discrepancy is the largest, the numerical results are approximately 30% of the values observed in experimental results. The test results for the axial force distribution differ considerably from those for the numerical distribution. This difference may have been due to uneven friction between the ground and the RBC model. Therefore, to verify the influence of friction, we conducted a sensitivity analysis in which we changed the friction conditions for the joint element; the axial force did not change much, and its distribution showed no significant variation. Thus, we believe that some other

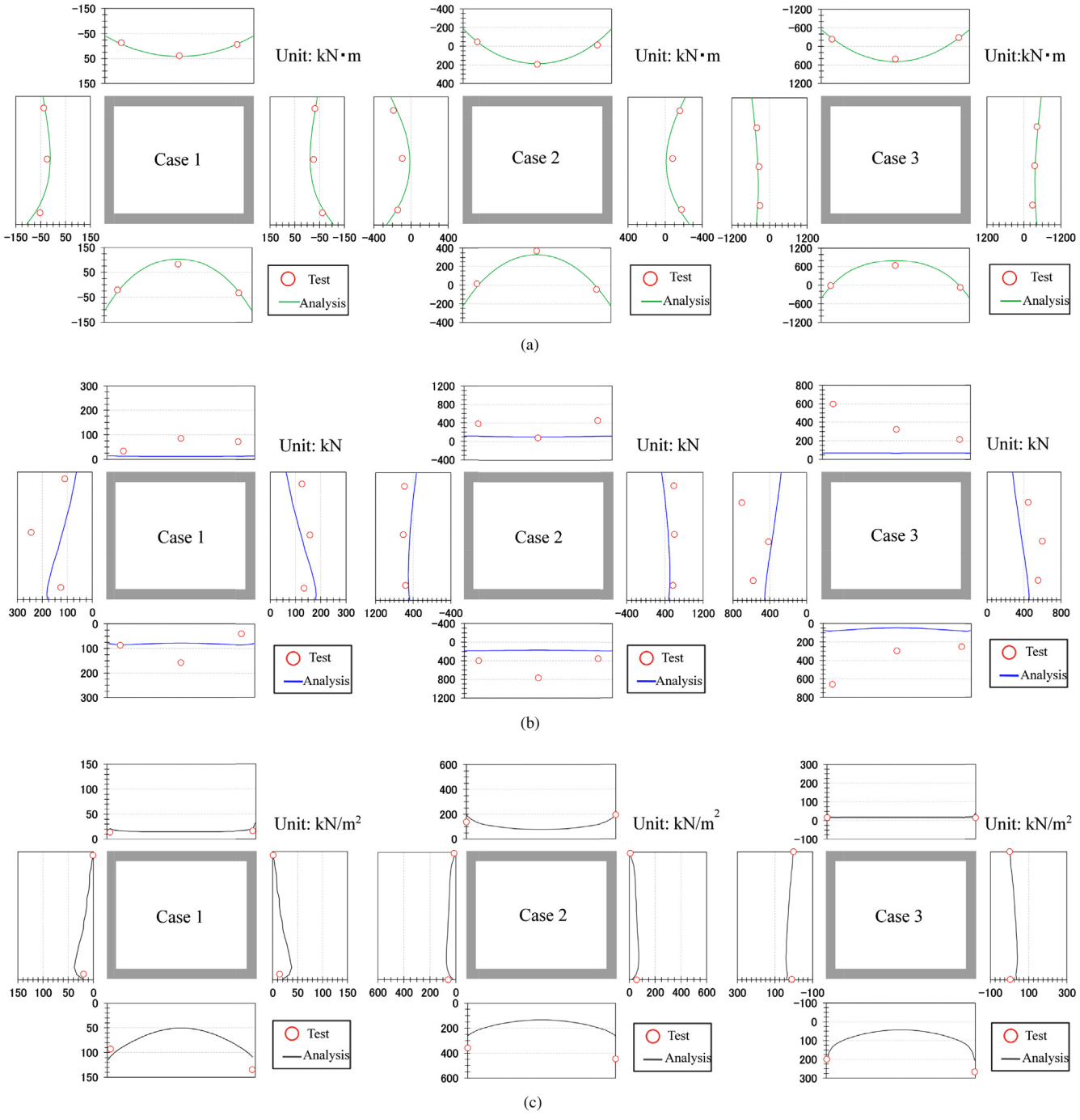

Fig. 16. Distributions of bending moment, axial force, and earth pressure in 1-g analysis: (a) bending moment (left: Case 1, center: Case 2, right: Case 3); (b) axial force (left: Case 1, center: Case 2, right: Case 3); and (c) earth pressure (left: Case 1, center: Case 2, right: Case 3).

factor caused the difference between the numerical and the experimental results, which is not quite clear at present.

Regarding the earth pressure distribution, the numerical analysis reproduced the experimental tests with reasonable accuracy in all cases. For the bottom slab in Case 2, which has a large overburden, the numerical results were lower than the experimental ones, but this difference is not as large as that for the axial force.

As shown in Fig. 16, the distributions of bending moment, axial force, and earth pressure do not show a symmetric shape. We assume that this can be attributed to the deficiency of setting up the culvert model in the ground.

4.2 Sectional force on culvert lining in dynamic analysis

Figure 17 shows the numerical and experimental results for the ground-strain time history under shaking. As mentioned previously, we obtained the ground strain from the relative displacement at a height between 7 m and 11 m. As

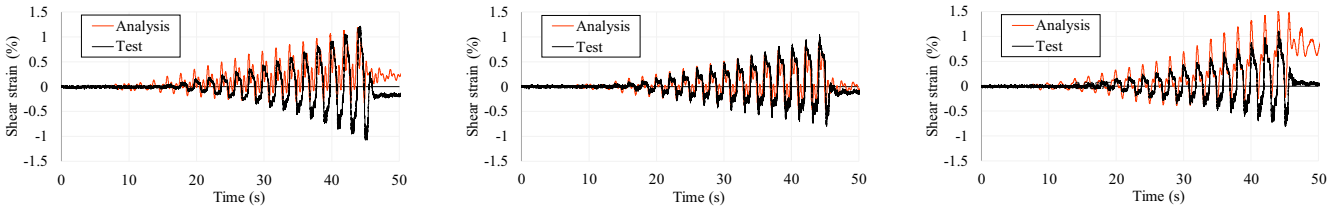

Fig. 17. Comparison of ground-strain time histories: (a) Case 1, (b) Case 2, and (c) Case 3. The ground strain obtained from the relative displacement at a height between 7 m and 11 m in the numerical and experimental results are compared herein.

shown, in Cases 1 and 3, the amplitudes of the positive and negative peaks increased gradually at almost the same rate, but in the analysis, the amplitude at the positive side exceeded that at the negative side, resulting in an amplitude history that is skewed to the positive side. In Cases 1 and 3, this trend occurs from the moment the shear strain reaches a shear strain of approximately 0.3% and the amplitude history becomes more skewed to the positive side as the shear strain increases. This phenomenon may have occurred because of the following: in the analysis, the amount of displacement on the positive side was larger than that on the negative side during one period, which generated discrepancy of displacement. This phenomenon occurs repeatedly, and the discrepancy is accumulated. Finally, the accumulation to the positive side caused the deviation of displacement to the positive side.

Regarding the numerical amplitudes of the shear strain on the positive and negative sides, in Case 3, they are almost the same as the experimental ones, whereas in Case 1, they are lower than the experimental ones after around the 30-s mark. No skewed amplitude was observed in Case 2, where a gradual increase on both sides was successfully reproduced. Moreover, the amplitude observed in the numerical results was approximately 90% of the value observed in the experimental results, with a shear strain of 0.5%. In addition, the amplitude observed in the numerical results was approximately 75% of the value observed in the experimental results, with a shear strain of 1.0%.

Regarding the variations in the bending moment, axial force, and earth pressure in the RBC under shaking, Fig. 18 shows the distributions of each case with a ground strain of 1.0% in the positive direction. Figure 19 compares the time-history responses of the numerical analysis and experimental results at the top and bottom of the left-sidewall, which is chosen as a representative member.

Regarding the bending moment, in Cases 1 and 2, the numerical results have a discrepancy of approximately ±10% from the experimental results. In Case 3, the left-sidewall is two times higher than that in the experiments. At other points, numerical results have a discrepancy of approximately ±15% from the experimental results. We attribute the large differences between the numerical and experimental results in Case 3 to the different positions at which the earth pressure and the external earthquake force act in the test and simulation models, as described in Section 1. These different positions generate the discrepancy of the total subjecting force and the position of the rotation center between them, and these factors may lead to different shear deformation and RR behaviors. In other words, the structural feature of the RBC lowers the numerical accuracy.

Regarding the axial force, RBCs with a wide cross-section, which is a structural feature of RBCs, have thick members, such as those in Case 3. In other words, the accuracy of the numerical analysis for RBCs with a wide cross-section became lower. The difference is especially large at the top and bottom slabs, where approximately 30% of the experimental results are same as numerical results. Moreover, the analysis cannot reproduce the distribution generated at the left-sidewall in Case 1 and the bottom slab in Cases 1 and 2. At this point, it is difficult to determine why this axial force causes the numerical and experimental results to differ. We must determine how this difference influences the evaluation of RBC earthquake behavior. On the sidewall, although we were unable to reproduce the axial force distribution shape accurately in each case, we were mostly successful at evaluating the average axial force within this member.

Regarding the earth pressure with a ground strain of 1.0%, the numerical result is almost 60% of the value of the experimental one in all cases. From the time-history analysis results, the numerical results are smaller than the experimental ones during the time when the ground strain is quite small. This result showed that the reproducibility of earth pressure is lower than that of the bending moment.

4.3 Shear strain distribution of ground

A distribution chart of shear and volume strains is created for a detailed analysis of the ground behavior under seismic motion. Figure 20 shows the shear and volume strain distributions of all cases with a ground strain of 1.0% in the positive direction. The left figure shows the shear strain distribution, and the right figure shows the volume strain distribution. Furthermore, the shear and volume strains are set at 5% (max). However, there are some elements which generate strains >5% because it is difficult to compare the results of 3 cases if the maximum strains in all of them are set to the maximum value of the distribution chart.

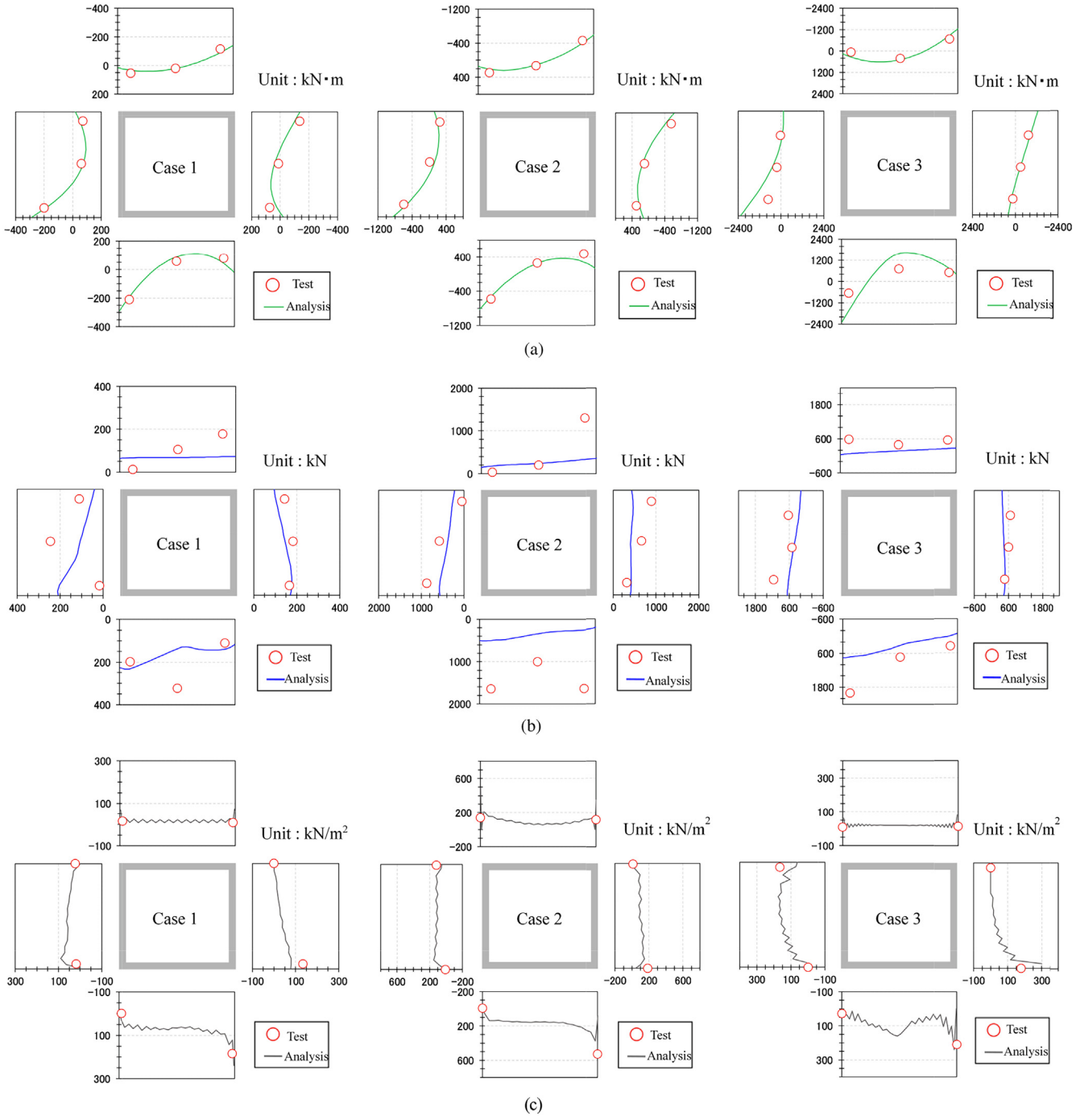

Fig. 18. Comparisons of experimental and numerical results for bending moment, axial force, and earth pressure: (a) bending moment (left: Case 1, center: Case 2, right: Case 3); (b) axial force (left: Case 1, center: Case 2, right: Case 3); and (c) earth pressure (left: Case 1, center: Case 2, right: Case 3).

In all cases, a shear strain of >5% was generated in some elements that were next to both the edges of the top slab. Ground elements under which there is no RBC show the subsidence, while ground elements under which there is RBC do not show the subsidence. Ground elements around both edges of the top slab are located between the areas that show subsidence and no subsidence, and become the transition area. Therefore, the large shear strain occurred in the transition area. Furthermore, the ground adjacent to the RBC sidewalls generated a large shear strain >5% in Cases 1 and 2. The earth pressure in the normal direction of sidewalls was <100 kN/m^2, >100 kN/m^2, and close to 200 kN/m^2 in Cases 1, 2, and 3, respectively. From these results, it is found that the shear strain of the ground next to the RBC sidewalls, where large earth pressure (over 100 kN/m^2) is generated, have a large value. However, large shear strain is generated around the bottom corner of sidewalls in the wide range only in Case 3. We assumed

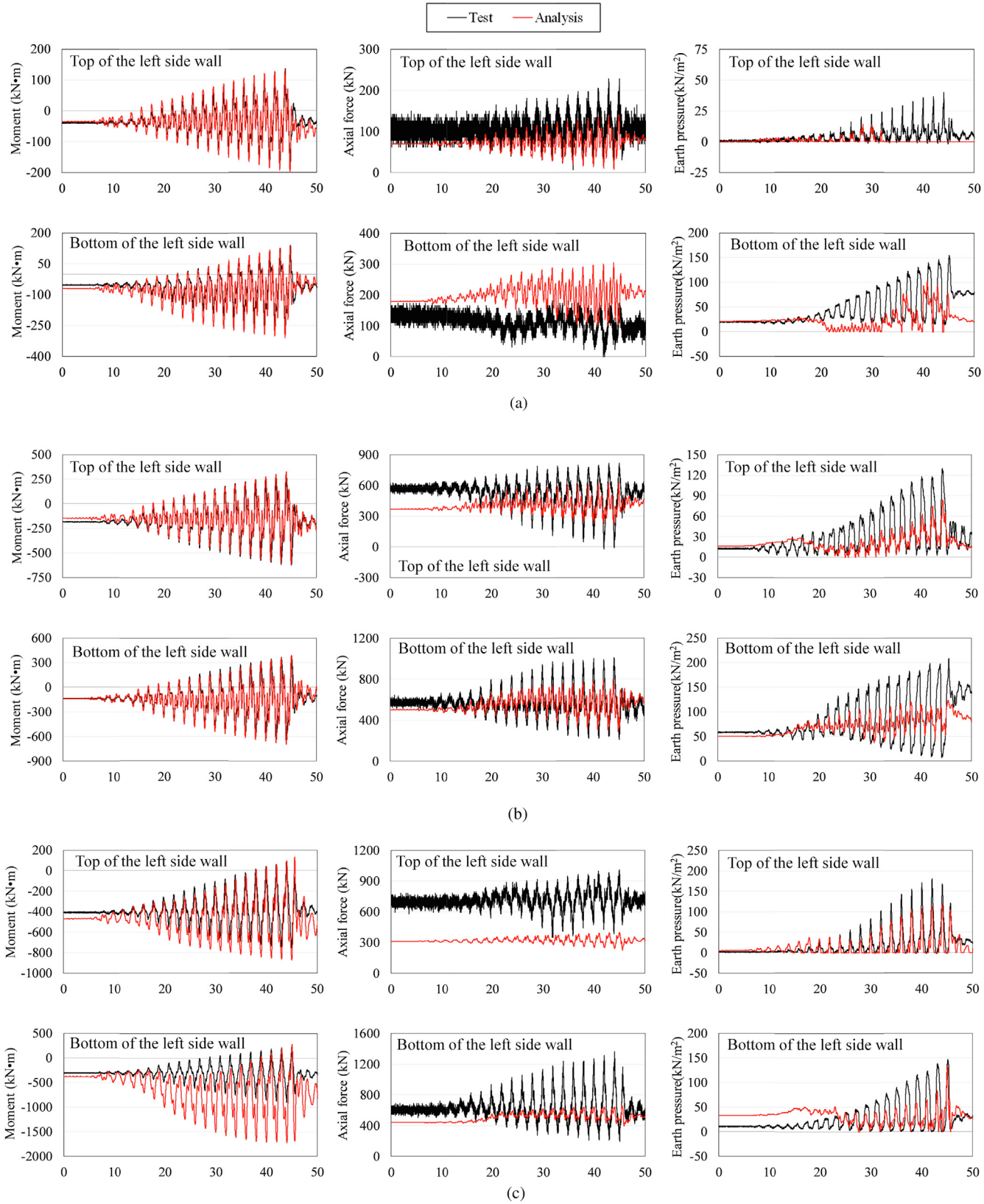

Fig. 19. Comparisons of experimental and numerical results for time-history responses of bending moment, axial force, and earth pressure: (a) Case 1 (left: bending moment, center: axial force, right: earth pressure); (b) Case 2 (left: bending moment, center: axial force, right: earth pressure); and (c) Case 3 (left: bending moment, center: axial force, right: earth pressure).

that the reason for this large strain in the wide range in Case 3 is a different shear deformation mode caused from the short distance between RBC and shear-chamber sidewalls. It is assumed that this large strain generated around the bottom corner of sidewalls leads to the overestimation of bending moment at the bottom and both end of sidewalls and bottom slab, respectively.

The volume strain of elements located above both edges of the top slab in both Cases 1 and 3 (shallow overburden case) undergoes expansion. However, the volume strain of elements located just next to (not above) both the edges of the top slab in Case 2 (large overburden case) stays compressed. Lateral and vertical shear deformations occur in the ground element located above both the sidewalls; therefore, the volume strain in those elements undergoes dilation (negative volume strain). In case of shallow overburden, the compressive volume strain (positive strain) is small from the initial state because of the small earth pressure, and the variation to the negative value of volume strain under shaking is larger than the initial compressive volume strain; hence, the volume strain reaches the expansion (negative) volume strain. However, in case of large overburden, the compressive volume strain (positive strain) is large from the initial state because of the large earth pressure and because the variation to the negative value of volume strain under shaking is smaller than the initial compressive

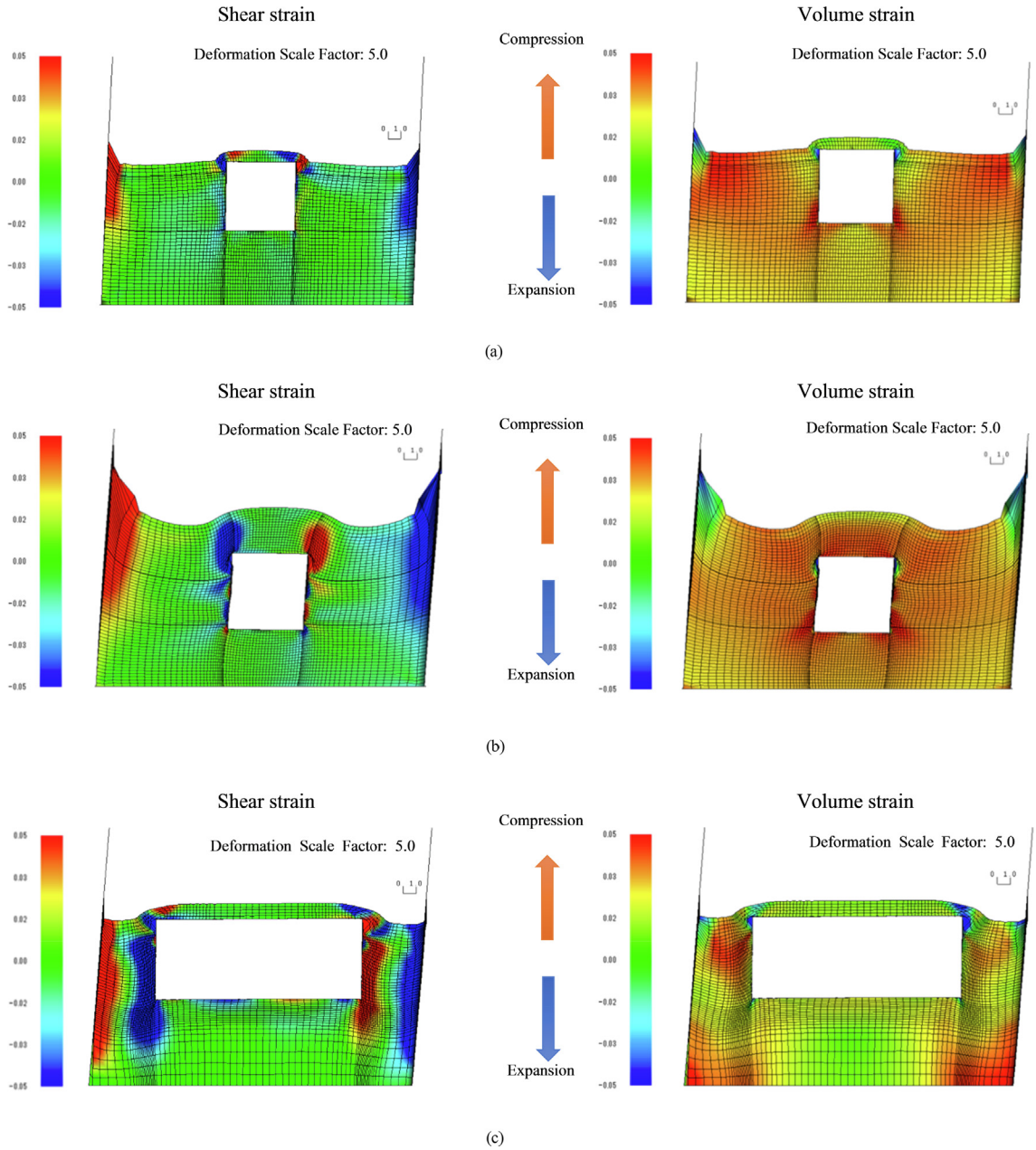

Fig. 20. Shear and volume strain distributions (ground strain of 1.0% in the positive direction): (a) Case 1 (left: shear strain, right: volume strain); (b) Case 2 (left: shear strain, right: volume strain); and (c) Case 3 (left: shear strain, right: volume strain).

volume strain, hence the volume strain does not reach the expansion (negative) volume strain. The compressive volume strain of elements located below both the edges of the bottom slab and next to the bottom of sidewalls undergo >5% increase in Cases 1 and 2. When RBCs adjust the RR, both the edges of the bottom slab become the center of rotation. Both the edges of bottom slab as the center of rotation were pushed into the ground because of the RR. Hence, the compressive volume strain of elements that are around both the edges of bottom slab increases. However, the volume strain of the element located below both the edges of the bottom slab and next to the bottom of the sidewalls does not show a large increase (<2% strain) in Case 3. RR angle in Case 3 is approximately half of that in Cases 1 and 2. We assume that this causes the small compressive volume strain in Case 3.

4.4 Analysis of shear deformation and rigid body rotation

As mentioned before, we conclude from the present experimental results that RR occurred in each case. As shown in Fig. 21, it is possible that shear deformation and RR occurred simultaneously during shaking, but these behaviors cannot be measured directly with a test. Therefore, we decided to determine the shear deformation angle and RR angle numerically.

The RR angle β occurs between the bottom slab and the foundation ground located beneath it. Based on the coordinates of the four corners of the RBC shown in Fig. 21, the shear deformation angle and the RR angle were derived from

$$\tan\beta = (y_4 - y_3)/W \tag{3}$$

$$\tan(\alpha+\beta) = (x_1 - x_4)/H \tag{4}$$

$$\alpha = \arctan(\alpha+\beta) - \arctan\beta \tag{5}$$

where x_1–x_4 are the x-coordinates of the RBC corners, y_1–y_4 are the y-coordinates of the RBC corners, W is the RBC width, H is the RBC height, and α is the shear deformation angle.

As described in the previous section, input motion used in this test comprises 20 periodic sine waves of 0.5 Hz. It is assumed that the response data of ground and RBCs differ in each period because the sine waves were gradually increased. Therefore, different response data in each period can be obtained if we divide the response data into 20 periods, as shown in Fig. 22. We also analyze the shear deformation angle α and RR angle β of each wave.

Figure 23 shows the time-history variation in the shear deformation angle α and RR angle β for each case, and Fig. 24 shows the relationship between the maximum input acceleration and the ratio of the maximum shear deformation angle α to the maximum RR angle β in each of the 20 waves. In Fig. 21, the maximum ground strain that occurred with each wave is also extracted and added to the figures.

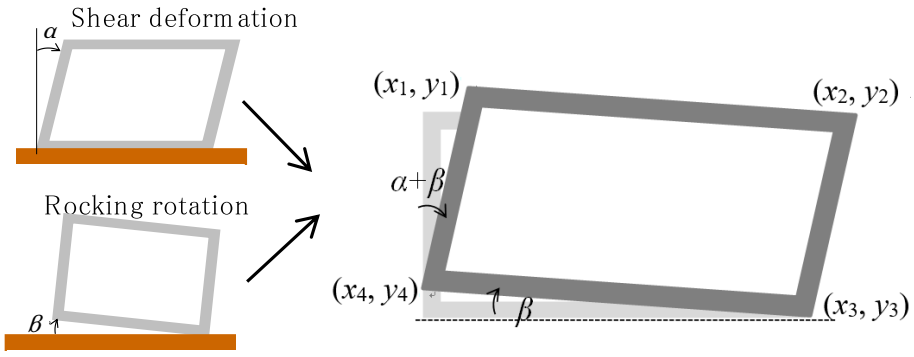

Fig. 21. Schematic of shear deformation and rocking rotation (RR).

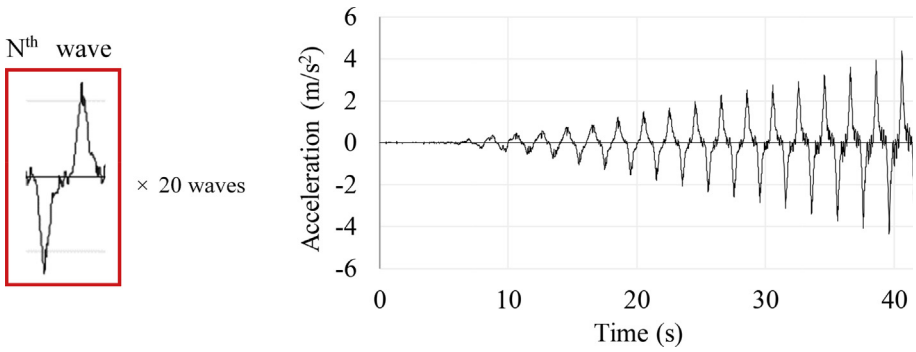

Fig. 22. Outline of the gradually increasing sine wave.

As shown in Fig. 24, in each case, the shear deformation angle α increases as the input acceleration increases. However, until the input acceleration exceeds approximately 0.8 m/s^2, the RR angle β remains very small. This indicates that when the shaking level is small, the RR is very small and both the surrounding ground and the RBC show the same shear behavior without no-contact state. After exceeding an input acceleration of approximately 0.9 m/s^2 (although there is a variation of input acceleration, e.g., 1.0 m/s^2 in Case 1, 0.8 m/s^2 in Case 2, and 0.7 m/s^2 in Case 3), the RBC shows RR and shear deformation with the noncontact sate between the ground and RBC is assumed to occur. However, it is difficult to use the acceleration to specify when the RR increases rapidly because there is a variation among the three cases. Meanwhile, regarding the ground strain shown in Fig. 25, the RR starts to increase sharply when the ground strain exceeds approximately 0.08%. These results suggest a correlation between the surrounding ground strain and the RR angle as well as between the surrounding ground strain and the shear deformation angle.

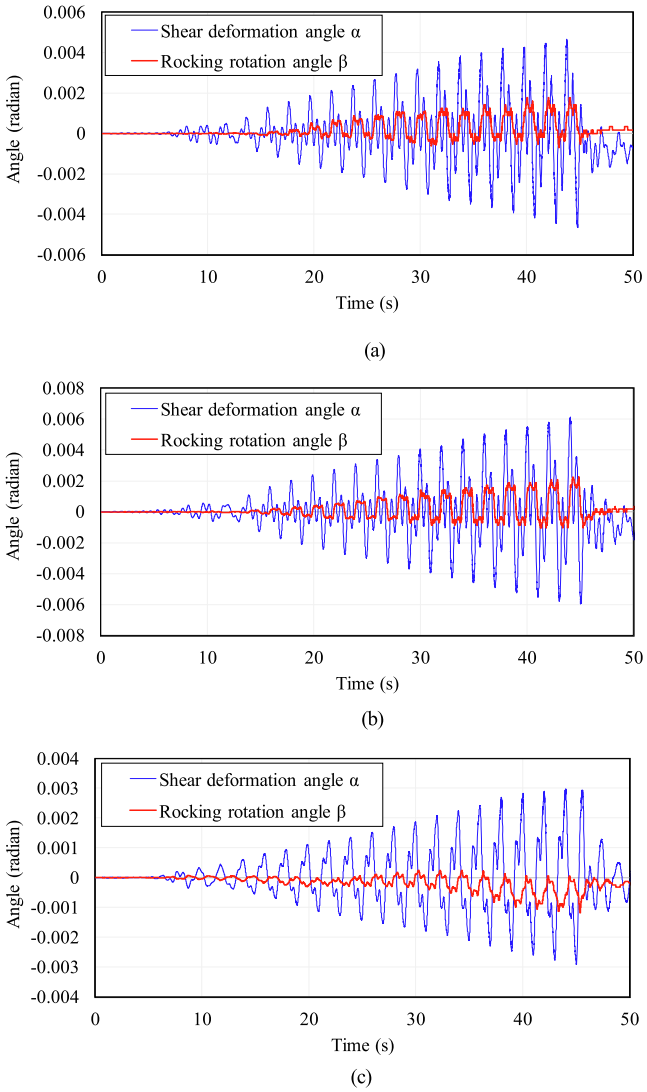

Fig. 23. Time-history behavior of shear deformation angle α and RR angle β in (a) Case 1, (b) Case 2, and (c) Case 3.

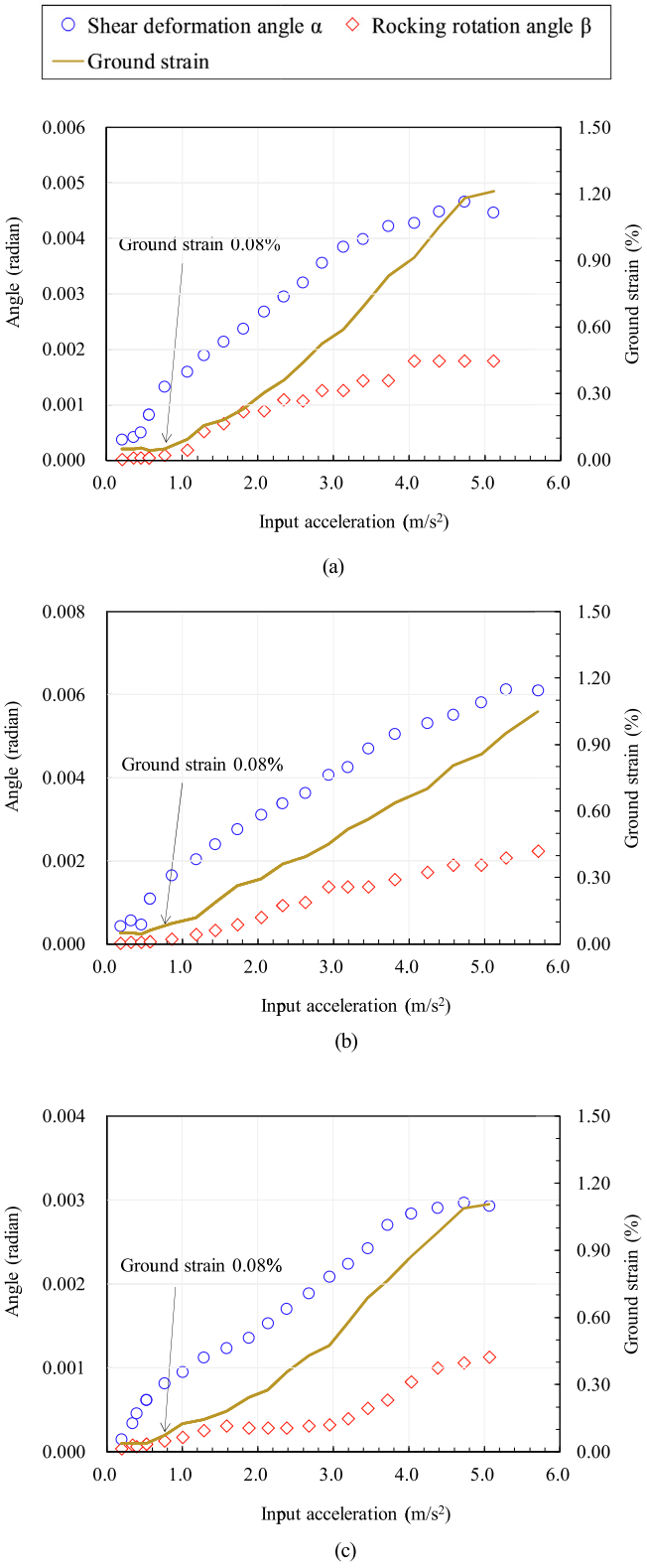

Fig. 24. Relationships between input acceleration, ground strain, shear deformation angle α, and RR angle β: (a) Case 1, (b) Case 2, and (c) Case 3.

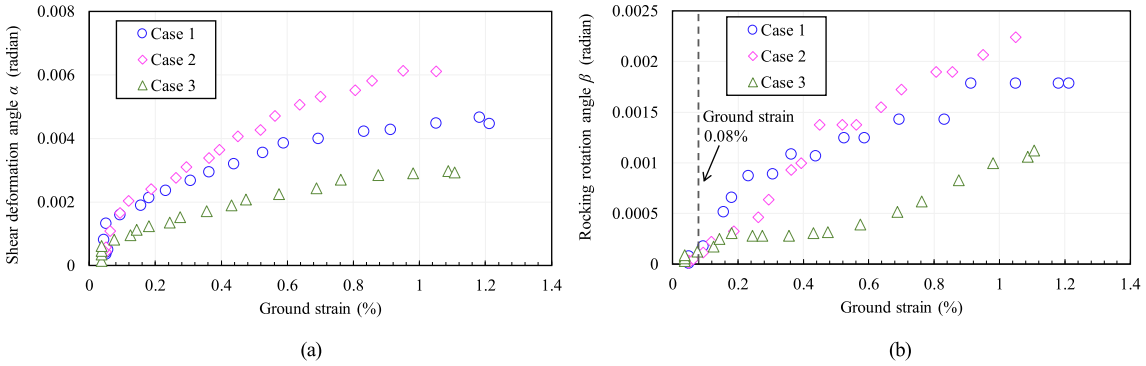

Fig. 25. Correlation with ground strain: (a) shear deformation angle α and (b) RR angle β.

Many researchers have reported a relationship between the surrounding ground strain and the shear deformation angle, namely, the racking ratio–flexibility ratio relationship (Abuhajar et al., 2015; Debiasi et al., 2013; Huo et al., 2006; Hushmand et al., 2016; Penzien, 2000; Tsinidis et al., 2016; Tsinidis, 2017; Wang, 1993). Racking ratio equals the structure shear strain over the ground shear strain. Therefore, these results show that there is a relationship expressed in the equation between them. Among these researchers, Tsinidis (2017) showed the relationship between the surrounding ground strain and the RR angle as the θ/γ_{ff}–flexibility ratio relationship obtained from the numerical analysis. θ/γ_{ff} equals the RR angle over the ground shear strain. Therefore, this result shows that there is a relationship expressed in the equation between them as with the structure shear strain. Based on these findings of these previous studies, we specially focus on the relationships among the maximum ground strain, the maximum shear deformation angle α, and the maximum RR angle β in each of the 20 waves. As shown in Fig. 25(a), despite the differences among the cases, the correlation between the surrounding ground strain and the shear deformation angle α is quadratic and quite strong. Meanwhile, from Fig. 25(b), after the ground strain exceeds 0.08%, the RR angle β increases sharply with the ground strain. However, the correlation between the surrounding ground strain and RR angle β is not as strong as that between the surrounding ground strain and the shear deformation angle α because there is dispersion in each wave. In Case 3, the correlation between the surrounding ground strain and the RR angle β is not shown and the dispersion in each wave is larger than that in other two cases. We assume that the discrepancy of correlation between Cases 1 & 2 and Case 3 is caused by the short distance between the soil chamber wall and RBC sidewall, so is the larger dispersion in Case 3.

Then, to determine the correlation between the maximum shear deformation angle α and the maximum RR angle β in each of the 20 waves, we construct a correlation diagram between the two indices, as shown in Fig. 26. All cases do not show a relationship as strong as the linear relationship between shear deformation angle α and RR angle β. This is caused by the dispersion in RR angle β, as shown in the correlation between the ground strain and angle β.

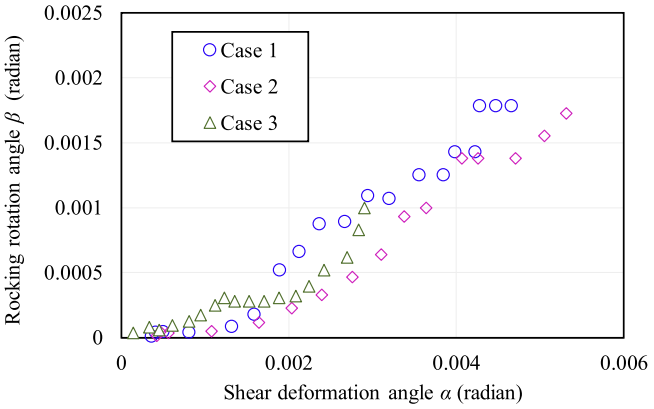

Fig. 26. Correlation between shear deformation angle α and RR angle β.

4.5 Considerations about numerical analysis

As mentioned in the preceding paragraph, the numerical results for the bending moment agree well with the experimental results, except in Case 3, which has a wide cross-sectional shape. In addition, the numerical axial forces were smaller than the experimental ones in each case, especially at the top and bottom slabs. As we were unable to determine the reason for this difference, we think that the proposed simulation has a tendency of underestimation of the compressive axial force. Therefore, the influence on the seismic behavior from this underestimation of compressive axial force was verified via numerical analysis. One of the most important factors when evaluating RBC's seismic behavior is the amount of shear deformation. When an RBC shows shear deformation, the sidewalls are the main members that resist the seismic force. Therefore, we used nonlinear pushover analysis employing the AFD model described in Section 2 to conduct sensitivity analysis in which we changed the axial forces acting on the sidewalls. We chose Case 2 as the analytical object because the difference in the axial force at the sidewall between the experimental and the numerical results was the largest of the

three cases (the numerical results of compressive axial force at the side in Case 2 were approximately 70% of the values obtained in experimental results).

Figure 27 shows the relationship between the horizontal displacement and the horizontal load in Case 2. The basic case shown in the figure refers to a case in which the axial force was not reduced. When the horizontal load is smaller than approximately 10 mm, there is barely any discrepancy in the relationship between horizontal displacement and horizontal load in both cases. However, when the horizontal displacement reaches approximately 15 mm and the response displacement begins to show a nonlinear response, the horizontal displacement in the case with a small axial force becomes larger than that in the basic case. This result shows that the lateral stiffness in the case with a low axial force becomes lower than that in the basic case.

Therefore, we focus on the lateral stiffness and summarize it based on the analysis results. Table 8 lists the lateral stiffness for horizontal displacements of 15, 29, and 58 mm. In the case with a reduced axial force, the decrease in stiffness is not large; only a 3% reduction appears even when the horizontal displacement reaches 58 mm. We believe that this small axial force does not significantly influence the lateral stiffness. Furthermore, we confirm the influence on the lateral stiffness from the small compressive axial force in Cases 1 and 3 via the same analysis. Similar results in the two cases were obtained.

Many researchers have proposed simplified seismic methods for underground structures (Abuhajar et al., 2015; Debiasi et al., 2013; Huo et al., 2006; Hushmand et al., 2016; Penzien, 2000; Tsinidis et al., 2016; Tsinidis, 2017; Wang, 1993) and have shown the relative stiffness between a structure and the surrounding ground to be a key factor in the structural seismic response. From this knowledge, it is possible to understand that the influence on the shear deformation is not large under a small change in the lateral stiffness. Table 8 summarizes the stiffness for horizontal displacements of 15, 29, and 58 mm. In the case with a reduced axial force, the decrease in stiffness is not large; only a 3% reduction appears even when the horizontal displacement reaches 58 mm. We reason that this stiffness reduction does not significantly influence the seismic deformation of RBCs in the ground.

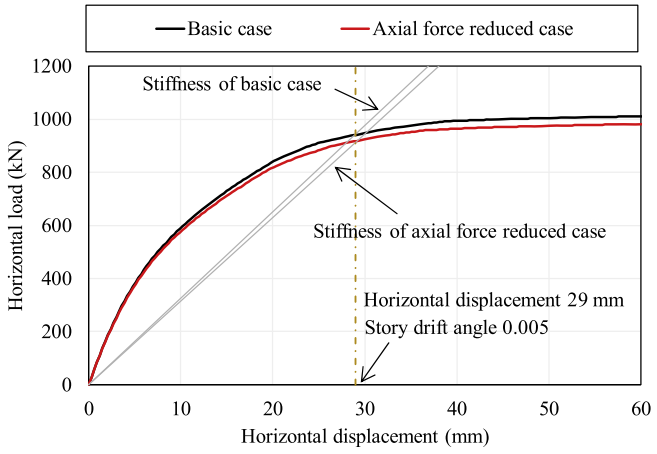

Fig. 27. Relationship between horizontal displacement and horizontal load in Case 2.

Table 8
Stiffness at several horizontal displacements.

Stiffness	Horizontal disiplacement (mm) (Story drift angle (radian))		
	15 (0.002 5)	29 (0.005 0)	58 (0.010)
① Basic case (kN/mm)	48.59	32.35	17.44
② Side walls axial force 70% (kN/mm)	47.86	31.55	16.93
②/①	0.98	0.98	0.97

From the series of analysis (reproduction analysis and analysis for the verification of the underestimation of the axial force), this simulation is capable of estimating the shear deformation with a certain accuracy, except in Case 3 (which involves a wide cross-sectional shape). In other words, in cases with a square cross section (Cases 1 and 2), the shear deformation behavior with approximately 90% accuracy can be estimated from the comparison between the bending moments in the experimental and numerical analysis results. However, the underestimated axial forces lead to overestimated tensile forces in the rebars and underestimated strength of the members. In other words, this simulation tends to easily judge the plastic yield and the shear failure of the members.

5 Conclusion

To verify the seismic behavior of the buried RBCs and establish a method for evaluating their seismic behavior, centrifuge model tests and a numerical analysis were carried out. In this test, we use the culvert model, the thickness of which was determined considering the nonlinear behavior of earthquake. In the structural condition, which we conducted in this experimental study, the main conclusions are summarized as follows:

(1) The test results show that as the earth pressure in the direction orthogonal to the axis of a member at the bottom slab increases with increased shaking, the earth pressure becomes zero (noncontact situation) after the ground strain exceeds 0.08%.
(2) Based on the acceleration and earth pressure measured in the present tests, RBCs will most likely develop RR when the ground strain is as small as 0.08%.
(3) A comparison of the numerical and experimental results shows that this analytical model can evaluate the bending moment accurately in cases with a square cross-section. Meanwhile, some discrepancies were observed: (i) the numerical axial forces were lower than the experimental ones in each case and (ii) the numerical bending moments were larger than the experimental ones in the case of wide cross-sections.

(4) From the sensitivity analysis in which the axial forces acting on the sidewalls were decreased, it was assumed that even though the seismic response obtained from this analysis tended to be overestimated under nonlinear behavior, the influence on the estimated seismic deformation was small. Therefore, it can estimate the shear deformation behavior with approximately 90% accuracy in square cross-section cases (Cases 1 and 2) judging from the comparison in the bending moment between the experiment and numerical analysis results. In addition, the underestimation of axial forces allowed us to easily estimate the plastic yield and the shear failure of the members.

(5) In the numerical analysis, a strong correlation appeared between the surrounding ground strain and the shear deformation angle calculated in Eq. (5). Moreover, the relationship between the RR angle and the surrounding ground strain did not appear to be as strong as that with the shear deformation angle.

The present study confirms that dynamic analysis can be used to evaluate the seismic behavior of RBCs. In future work, we will test other seismic methods (e.g., the simplified method and the response displacement method) that many previous researchers have used for the seismic design of underground structures. After evaluating those methods, we hope to suggest an appropriate seismic design method for RBCs.

Acknowledgements

During the design of the experimental models, GEOSTR Corporation provided insightful comments and suggestions.

References

Abuhajar, O., El Naggar, H., & Newson, T. (2015). Experimental and numerical investigations of the effect of buried box culverts on earthquake excitation. *Soil Dynamics and Earthquake Engineering, 79*, 130–148.

Cui, Y., Kishida, K., & Kimura, M. (2010). Analytical study on the control of ground subsidence arising from the phenomenon of accompanied settlement using footing reinforcement pile, *Deep and Underground Excavation* (pp. 307–312).

Danno, K., & Kimura, M. (2009). Evaluation of long-term displacements of pile foundation using coupled FEM and centrifuge model test. *Soils and Foundations, 49*(6), 941–958.

Debiasi, E., Gajo, A., & Zonta, D. (2013). On the seismic response of shallow-buried rectangular structures. *Tunnelling and Underground Space Technology, 38*, 99–113.

Eight-Japan Engineering Consultants Inc (2016). Report of the 2016 Kumamoto Earthquake Retrieved September 18, 2018, from http://www.ejec.ej-hds.co.jp/center/pdf/160712.pdf.

Hamada, M., & Ohmachi, T. (1996). Evaluation of earthquake-induced displacement and strain of the surface ground in near-field. *Hanshin-Awaji Dai-shinsai ni kansuru Gakujyutsu-Kouenkai ronbunsyuu*, 69–80 (in Japanese).

Huo, H., Bobet, A., Fernández, G., & Ramirez, J. (2006). Analytical solution for deep rectangular structures subjected to far-field shear stress. *Tunnelling and Underground Space Technology, 21*(6), 613–625.

Hushmand, A., Dashti, S., Davis, C., Hushmand, B., Zhang, M., Ghayoomi, M., ... Hu, J. (2016). Seismic performance of underground reservoir structures: Insight from centrifuge modeling on the influence of structure stiffness. *Journal of Geotechnology and Geoenvironment Engineering, 142*(7), 04016020.

Japan Road Associations (2010). *Design and Construction guiding principle for road earth works and culverts* (2010 Edition). Maruzen Print Co. Ltd (in Japanese).

Jin, Y., Bao, X., Kondo, Y., & Zhang, F. (2010). Soil-water coupling analysis of real-scale field test for 9-pile foundation subjected to cyclic horizontal loading. *Deep Foundation and Geotechnical In Situ Testing, 205*, 111–118.

Kimura, M., & Zhang, F. (2000). Seismic evaluations of pile foundations with three different methods based on three-dimensional elasto-plastic finite element analysis. *Soils and Foundations, 40*(5), 113–132.

Murakami, S. (2011). Report of the 2011 Great East Japan Earthquake, Retrieved September 18, 2018, from www.geo.civil.ibaraki.ac.jp/murakami/GIS/topics/TohokuTaiheiyo2011/IbadaiGeo201104N08-2.pdf.

Nakai, T., & Hinokio, M. (2004). A simple elastoplastic model for normally and over consolidated soils with unified material parameters. *Soils and Foundations, 44*(2), 53–70.

National Institute for Land and Infrastructure Management Ministry of Land and Public Works Research Institute (2004). Report on damage to infrastructures by the 2004 Mid Niigata Prefecture Earthquake. In Research report of National Institute for Land and Infrastructure Management, No. 27, January 2006. (in Japanese), Retrieved September 18, 2018, from http://www.nilim.go.jp/lab/bcg/siryou/rpn/rpn0027.htm.

Penzien, J. (2000). Seismically induced racking of tunnel linings. *Earthquake Engineering and Structural Dynamics, 29*, 683–691.

Sawamura, Y., Kishida, K., & Kimura, M. (2014). Evaluation of dynamic behavior of culverts and embankments through centrifuge model tests and a numerical analysis. *In Proc. of the 14th International Conference of the International Association for Computer Methods and Recent Advances in Geomechanics*, Kyoto (pp. 743–748).

Sawamura, Y., Ishihara, H., Kishida, K., & Kimura, M. (2016). Evaluation of damage morphology in three-hinge precast arch culvert based on shaking table tests and numerical analyses. *In Proc. of the 8th Young Geotechnical Engineering Conference, Astana*, Kazakhstan (pp. 221–226).

Sawamura, Y., Matsushita, R., Kishida, K., & Kimura, M. (2017). Study on aseismic design approach of two-hinge precast arch culvert through shaking table tests and numerical analyses. *In Proc. of the 15th International Conference of the International Association for Computer Methods and Recent Advances in Geomechanics*, No. 865, Wuhan, China.

Toyota, H. (2007). Report of the 2007 Niigata-ken Chuetsu-oki Earthquake, Retrieved September 18, 2018, from http://133.44.114.42/HTML/shear/.

Tsinidis, G. (2017). Response characteristics of rectangular tunnels in soft soil subjected to transversal ground shaking. *Tunnelling and Underground Space Technology, 62*, 1–22.

Tsinidis, G., Rovithis, E., Pitilakis, K., & Chazelas, J. L. (2016). Seismic response of box-type tunnels in soft soil: Experimental and numerical investigation. *Tunnelling and Underground Space Technology, 59*, 199–214.

Wang, J. N. (1993). Seismic design of tunnels: A state-of-the-art approach. Monograph 7. New York: Parsons Brinckerhoff Quade & Douglas.

Xia, Z. F., Ye, G. L., Wang, J. H., Ye, B., & Zhang, F. (2010). Numerical analysis on the influence of thickness of liquefiable soil on seismic response of underground structure. *Journal of Shanghai Jiaotong University, 15*(3), 279–284.

Yamaki, M., Tanimoto, S., & Sasaki, T. (2011). Dynamic centrifuge model tests on dynamic behavior of box culvert in large earthquake. In *Proceedings of the 56th Geotechnical Symposium* (pp. 303–310) (in Japanese).

Yatsumoto, H., Fujiwara, S., Hoshikuma, J., Taniguchi, T., Kitamura, T., & Tamakoshi, T. (2015). Evaluation of seismic limit state of single cell box culvert for road. *Journal of JSCE, Division A1 (Structural Engineering/Earthquake Engineering), 71*(3), 295–314 (in Japanese).

Ye, B., Ye, G. L., Zhang, F., & Yashima, A. (2007). Experiment and numerical simulation of repeated liquefaction-consolidation of sand. *Soils and Foundations, 47*(3), 547–558.

Zhang, F., & Kimura, M. (2002). Numerical prediction of the dynamic behaviors of an RC group pile foundation. *Soils and Foundations, 42*(3), 72–92.